

DTIC FILE COPY

4

GL-TR-89-0284

AD-A219 479

DEVELOPMENT AND USE OF DATA ANALYSIS PROCEDURES FOR THE CRRES  
PAYLOADS AFGL-701-2/DOSIMETER AND AFGL-701-4/FLUXMETER AND  
APPLICATION OF THE DATA ANALYSIS RESULTS TO IMPROVE THE STATIC AND  
DYNAMIC MODELS OF THE EARTH'S RADIATION BELTS

Bronislaw K. Dichter  
Frederick A. Hanser

PANAMETRICS, INC.  
221 Crescent Street  
Waltham, MA 02254

SCIENTIFIC REPORT NO. 2

12 October 89

Approved for Public Release; Distribution Unlimited

GEOPHYSICS LABORATORY  
AIR FORCE SYSTEMS COMMAND  
UNITED STATES AIR FORCE  
HANSCOM AFB, MASSACHUSETTS 01731-5000

DTIC  
ELECTE  
MAR 20 1990  
S B D

90 03 20 133

"This technical report has been reviewed and is approved for publication"

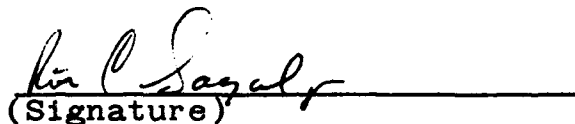


(Signature)  
MARILYN R. OBERHARDT  
Contract Manager



(Signature)  
E.G. MULLEN  
Branch Chief

FOR THE COMMANDER



(Signature)  
RITA C. SAGALYN  
Division Director

This report has been reviewed by the ESD Public Affairs Office (PA) and is releasable to the National Technical Information Service (NTIS).

Qualified requestors may obtain additional copies from the Defense Technical Information Center. All others should apply to the National Technical Information Service.

If your address has changed, or if you wish to be removed from the mailing list, or if the addressee is no longer employed by your organization, please notify GL/IMA, Hanscom AFB, MA 01731. This will assist us in maintaining a current mailing list.

Do not return copies of this report unless contractual obligations or notices on a specific document requires that it be returned.

REPORT DOCUMENTATION PAGE

1a. REPORT SECURITY CLASSIFICATION Unclassified		1b. RESTRICTIVE MARKINGS	
2a. SECURITY CLASSIFICATION AUTHORITY		3. DISTRIBUTION/AVAILABILITY OF REPORT Approved for public release Distribution unlimited	
2b. DECLASSIFICATION/DOWNGRADING SCHEDULE			
4. PERFORMING ORGANIZATION REPORT NUMBER(S)		5. MONITORING ORGANIZATION REPORT NUMBER(S) GL-TR-89-0284	
6a. NAME OF PERFORMING ORGANIZATION Panametrics, Inc.	6b. OFFICE SYMBOL (If applicable)	7a. NAME OF MONITORING ORGANIZATION Geophysics Laboratory	
6c. ADDRESS (City, State and ZIP Code) 221 Crescent Street Waltham, MA 02254		7b. ADDRESS (City, State and ZIP Code) Hanscom AFB Massachusetts 01731-5000	
8a. NAME OF FUNDING/SPONSORING ORGANIZATION	8b. OFFICE SYMBOL (If applicable)	9. PROCUREMENT INSTRUMENT IDENTIFICATION NUMBER F19628-87-C-0169	
8c. ADDRESS (City, State and ZIP Code)		10. SOURCE OF FUNDING NOS.	
		PROGRAM ELEMENT NO. 62101F	PROJECT NO. 7601
		TASK NO. 20	WORK UNIT NO. CF
11. TITLE (Include Security Classification) (SEE BACK)			
12. PERSONAL AUTHOR(S) Bronislaw K. Dichter and Frederick A. Hanser			
13a. TYPE OF REPORT Scientific #2	13b. TIME COVERED FROM _____ TO _____	14. DATE OF REPORT (Yr., Mo., Day) 12 October 89	15. PAGE COUNT 70
16. SUPPLEMENTARY NOTATION			
17. COSATI CODES		18. SUBJECT TERMS (Continue on reverse if necessary and identify by block number)	
FIELD	GROUP	SUB. GR.	
			Fluxmeter, Calibration, Electrons, Protons, (S)
19. ABSTRACT (Continue on reverse if necessary and identify by block number)			
<p>This report summarizes the calibration work done on the High Energy Electron Fluxmeter, an instrument to be flown aboard the Combined Release and Radiation Satellite (CRRES). The instrument was calibrated using electron beams with energies between 0.75 to 10.8 MeV and proton beams with energies between 25 and 144 MeV. <i>keywords</i></p>			
20. DISTRIBUTION/AVAILABILITY OF ABSTRACT UNCLASSIFIED/UNLIMITED <input checked="" type="checkbox"/> SAME AS RPT. <input type="checkbox"/> DTIC USERS <input type="checkbox"/>		21. ABSTRACT SECURITY CLASSIFICATION Unclassified	
22a. NAME OF RESPONSIBLE INDIVIDUAL Lt. M. R. Oberhardt		22b. TELEPHONE NUMBER (Include Area Code) (617) 377-3991	22c. OFFICE SYMBOL GL/PHE

11. Development and Use of Data Analysis Procedures for the CRRES Payloads AFGL-701-2/Dosimeter and AFGL-701-4/Fluxmeter and Applications of the Data Analysis Results to Improve the Static and Dynamic Models of the Earth's Radiation Belts

## TABLE OF CONTENTS

	<u>Page</u>
LIST OF ILLUSTRATIONS	iv
LIST OF TABLES	vi
1. INTRODUCTION	1
2. LOW ENERGY ELECTRON RESPONSE	1
2.1 Experimental Arrangement	3
2.2 Data Reduction	3
2.3 Experimental Results	7
2.4 Theoretical Analysis of the Fluxmeter Electron Response	12
2.4.1 Description of Fluxmeter Model	12
2.4.2 Model Calculations and Comparison with Data	18
3. HIGH ENERGY ELECTRON RESPONSE	20
3.1 Experimental Arrangement	24
3.2 Angular Distributions	24
3.3 Energy Distributions	26
3.4 Data Reduction	29
3.5 Experimental Results and Calculations	33
3.5.1 Total Geometric Factor	33
3.5.2 Energy Channel Response Calculation	33
4. SUMMARY OF ELECTRON CALIBRATION RESULTS	36
5. PROTON RESPONSE MEASUREMENT	39
5.1 Singles Data	39
5.2 Coincidence Data	49
6. CONCLUSION	55
REFERENCES	57
APPENDIX	58

	n For
	A&I <input checked="" type="checkbox"/>
	ced <input type="checkbox"/>
	ation <input type="checkbox"/>
	tion/
	ility Codes
.Dist	Avail and/or Special
A-1	

## LIST OF ILLUSTRATIONS

<u>Figure</u>	<u>Title</u>	<u>Page</u>
1.1	Cross Section of High Energy Electron Fluxmeter	2
2.1	Rate Meter Dead Time as a Function of Input Count Rate	4
2.2	Geometric Factor as a Function of Electron Energy for the First Three Electron Channels and their Sum	8
2.3	Ratio of LL-L1 Channel Counts to the Sum of Counts in the LL-L1 and L1-L2 Channels	9
2.4	Count Rate at 0° Relative to the Count Rate with HV-128	13
2.5	Fraction of the Total Fluxmeter Counts that are Recorded in a Given Electron Channel	14
2.6	Angular Distributions from Electron Multiple Scattering	16
2.7	Ratio of Triple Coincidence Counts to Double Coincidence Counts	19
2.8	Effective Area of SSD-Front	21
2.9	Effective Area of SSD-Back	22
2.10	Effective Area of the BGO Scintillator	23
3.1	Measured Angular Distributions at RADC and GSFC	27
3.2	Standard Deviation $\sigma_a$ used in eq. (3.1)	28
3.3	Standard Deviation $\sigma_b$ used in eq. (3.1)	28
3.4	Measured and Calculated Fluxmeter Energy Spectron	30
3.5	Effective SSD-F Area	32
4.1	Total Fluxmeter Geometric Factor	37
4.2	Absolute Response of Fluxmeter Channels LL-L1 thru L6-L7	40
4.3	Absolute Response of Fluxmeter Channels L6-L7 thru L9-L10	41

## LIST OF ILLUSTRATIONS

<u>Figure</u>	<u>Title</u>	<u>Page</u>
5.1	Ratio of Counts of SSD-Front to SSD-Back Detectors	42
5.2	Effective BGO Crystal Area with the Fluxmeter at $0^\circ$ with Respect to the Beam	45
5.3	Measured BGO Crystal Area as a Function of Fluxmeter Angle	46
5.4	Fraction of the Total BGO Counts Found in the two Lowest and the Highest BGO Pulse Height Channels	47

## LIST OF TABLES

<u>Table</u>	<u>Title</u>	<u>Page</u>
2.1	Effective Area of the Three Lowest Fluxmeter BGO Channels as a Function of Electron Energy	10
2.2	Geometric Factors for the Three Lowest Fluxmeter Electron Channels	11
2.3	Listing of Aperture and Aperture Panameters Used in the Fluxmeter Simulation Calculation	17
3.1	List of Energies and Angles Investigated at the RADC Linar	25
3.2	Geometric Factors Calculated Using Methods of Section 3.5.1	34
4.1	List of Geometric Factors from GSFC and RADC Experiments	38
4.2	List of Parameters used in egs. (4.2) and (4.3) to Describe the Response of the Fluxmeter Energy Channels	43
5.1	Measured and Calculated areas of the Fluxmeter at $0^\circ$ to the Proton Beam	48
5.2	Measured Distribution of Counts in the BGO Channels Averaged for Sums with Beam Energies Between 51 and 144 MeV	50
5.3	Fluxmeter Geometric Factors for CRF ON	51
5.4	Fluxmeter Proton Geometric Factors for CRB ON	52
5.5	Fluxmeter Proton Geometric Factors for CRF and CRB ON	53
5.6	Fluxmeter Proton Geometric Factors for all Coincidence ON	54
5.7	Listing of $F_c$ Values, and the Geometric Information Used to Derive them, for the Various Beam Energies and Coincidence Modes	56

## 1. INTRODUCTION

This report contains the description and results of the calibration of the High Energy Electron Fluxmeter. The Fluxmeter was designed to detect, in orbit, electrons with energies between 1 and 10 MeV and be insensitive to protons with energies up to several hundred MeV. A full description of this instrument can be found in Ref. 1.1. The Fluxmeter was built for the Air Force by Panametrics under contract F19628-79-C-1075. The calibration work was carried out under contract F19628-82-C-0090. (See Ref. 1.2), while the final analysis of the calibration data was carried out under contract F19628-87-C-0169.

The Fluxmeter is shown in cross section view in Fig. 1.1. Electrons are detected using two solid state silicon surface barrier detectors (SSD's) and a bismuth germanate (BGO) scintillator. An annular plastic scintillator surrounds the BGO crystal, and is used in anti-coincidence to reduce the response to high energy penetrating protons and to electrons which scatter out of the BGO crystal. The two SSD coincidences and the shield anti-coincidence can be enabled or disabled individually by ground command. The basic operating modes and theoretical energy loss curves are discussed in detail in Ref. 1.1. The present report is concerned primarily with the analysis and presentation of the Fluxmeter calibration data.

All the accelerator calibration work done on the Fluxmeter is discussed in this report. The summary of the electron calibration results is in Section 4, while the summary of the proton tests is in section 5. Sections 2 and 3 contain the details of the electron calibration work and have been included for the sake of completeness. Section 2 contains the results of the low energy electron, 0.75 to 1.75 MeV, calibration done at the Goddard Space Flight Center Van de Graaff accelerator. Section 3 is a report on the high energy electron, 1.3 to 10.8 MeV, calibration carried out at the Rome Air Development Center LINAC at the Hanscom Air Force Base. Sections 2 and 4 have been adopted from the final report for contract F19628-82-C-0090 (AFGL document GL-TR-89-0152), Ref. 1.2.

## 2. LOW ENERGY ELECTRON RESPONSE

The low energy electron response of the Fluxmeter was studied in tests performed at Goddard Space Flight Center (GSFC) electron accelerator in July, 1987. Beams of electrons with energies ranging from 0.25 to 1.75 MeV and angles of incidence between  $0^\circ$  and  $30^\circ$  were used to bombard the instrument. The experimentally determined quantities were the count rates of the two solid state detectors, SSD-Front and SSD-Back, and the BGO scintillator. The measurements were taken as a function of beam energy, angle of incidence of the beam and the high voltage applied to the photomultiplier tube viewing the BGO crystal. Sections 2.1 through 2.3 contain a discussion of the data reduction and a summary of the

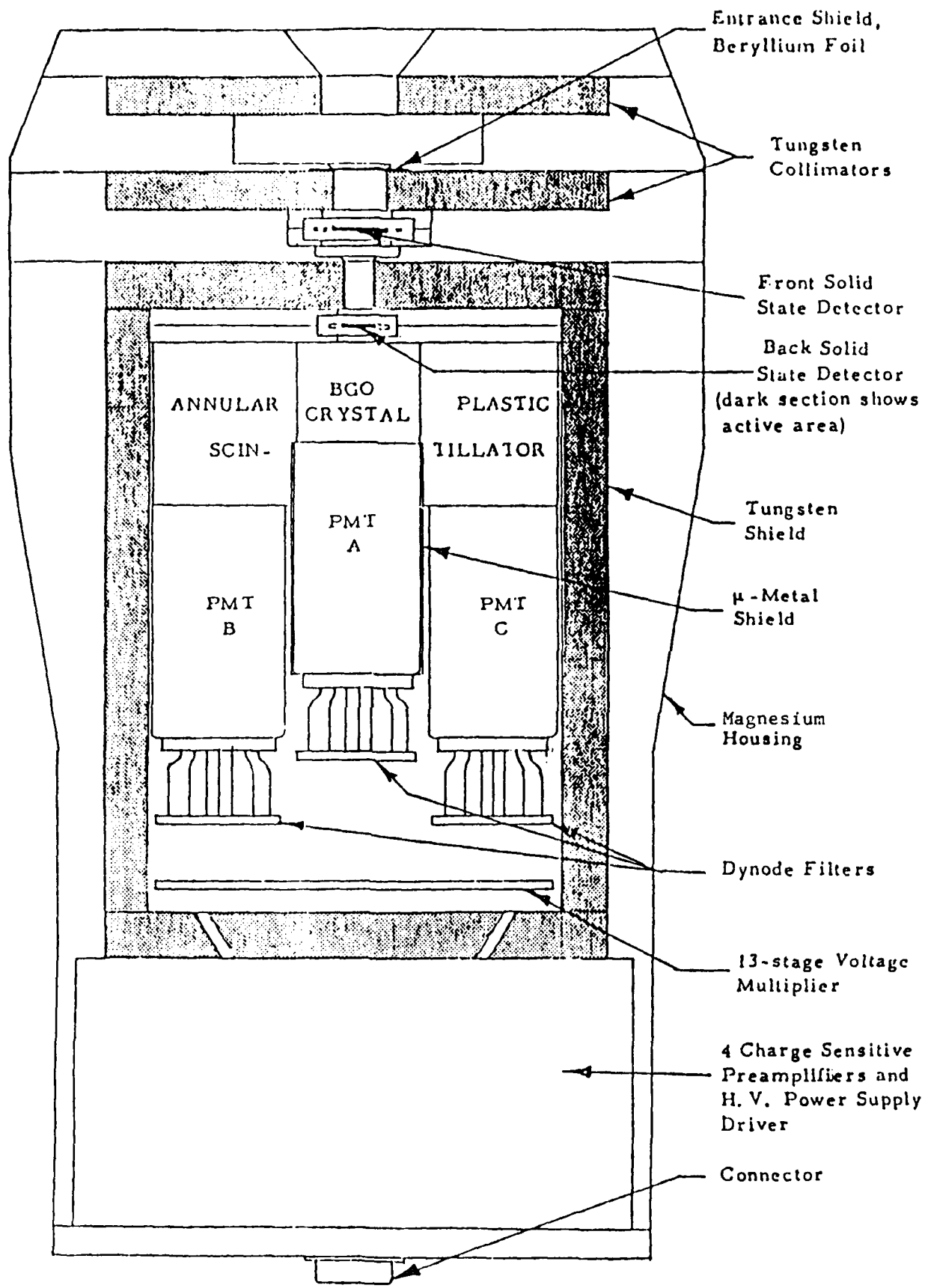


Fig. 1.1. Cross Section of High Energy Electron Fluxmeter.

results. A theoretical calculation of the expected response of the instrument and a comparison with the data are included in Section 2.4.

## 2.1 Experimental Arrangement

During the tests at GSFC, the Fluxmeter was mounted on a rotating table, whose orientation with respect to the beam axis could be varied and accurately determined. The pivot point of the rotation of the Fluxmeter was a point along the axis of cylindrical symmetry of the telescope and located half way between the two solid state detectors. During the tests, the Fluxmeter was rotated from  $+30^\circ$  to  $-21^\circ$  with respect to the electron beam.

Beam spot size was set by a  $1.27 \text{ cm}^2$  area collimator at the entrance to the chamber containing the Fluxmeter. A phosphor was observed visually to allow focus adjustments to produce a uniform intensity over the entire spot area. Subsequently, beam intensity was measured with solid state monitor detector connected to a ratemeter. The area of the monitor was chosen to be larger than the collimated beam spot. The monitor was moved into the beam frequently between Fluxmeter tests so that the interpolated monitor count rate could provide a normalization for each Fluxmeter measurement.

## 2.2 Data Reduction

Fluxmeter data were collected in 10 second long intervals. Eight such intervals constituted a data record. The beam intensity was measured every 2 to 3 records. Linear interpolation of the measured values was used to associate a beam intensity with each record, or fraction of record. The ratemeter reading was accurate to better than 3% at all times. Ratemeter dead time as a function of beam intensity, was measured and found to be a small correction, of the order of 3 - 5% for most of the data of interest (see Fig. 2.1). Thus, the estimated record-to-record relative normalization error, including the interpolation error, is of the order of 7%.

For measurements with non-zero angles of beam incidence the beam spot geometry must be considered. The pivot point of Fluxmeter rotation was such that, when the instrument was rotated to an angle  $\theta$ , the entrance aperture of the telescope moved horizontally away from the beam axis. The distance of the center of the entrance aperture from the beam axis,  $D$ , is just

$$D = D_p \sin(\theta) \quad (2.1)$$

where  $D_p = 3.94 \text{ cm}$  is the distance from the pivot point to the entrance aperture. If the beam spot is of the same size as the entrance aperture of the fluxmeter, as was evidently observed, then the rotation of the instrument has the effect of moving a

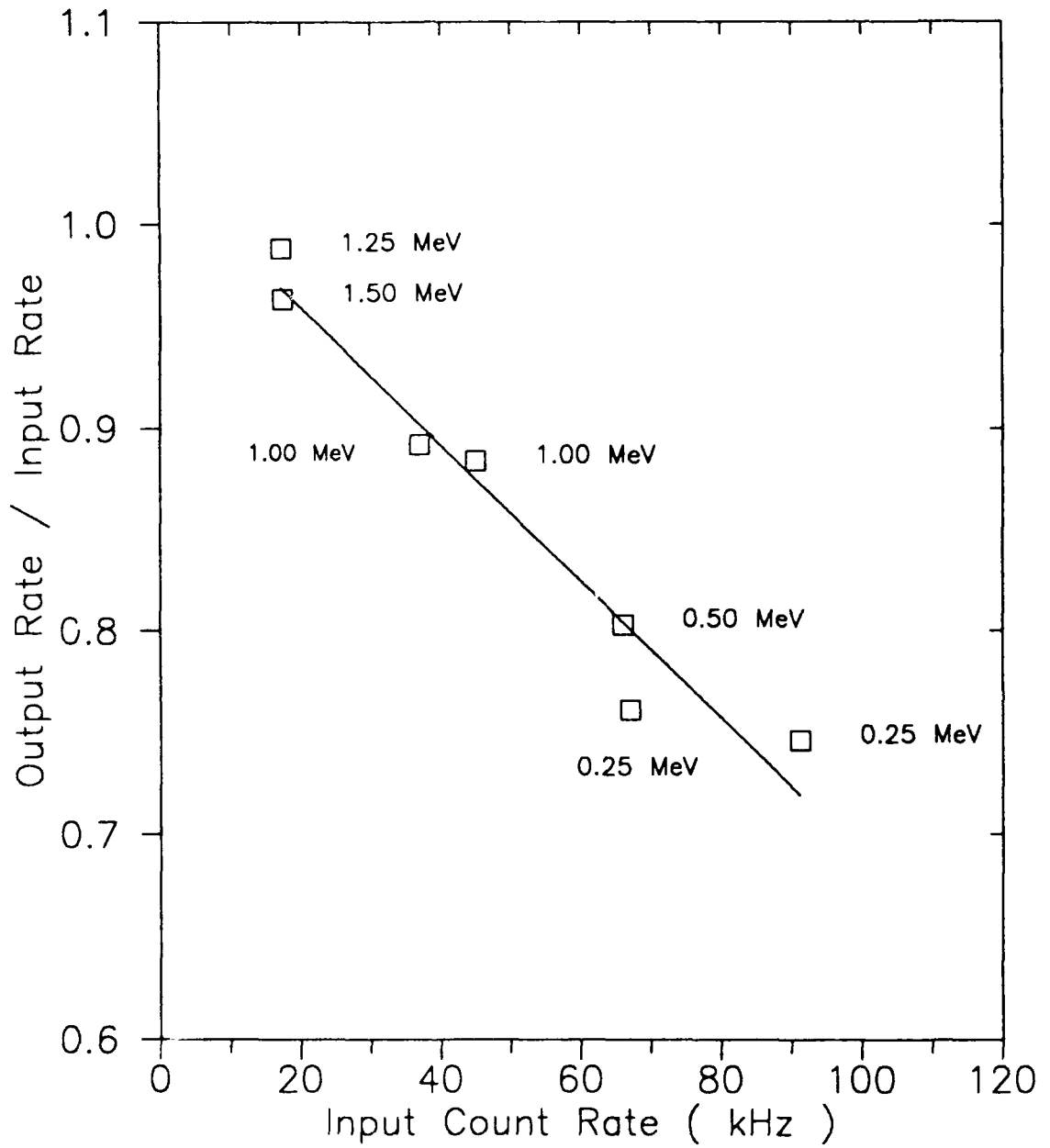


Figure 2.1 Rate meter dead time as a function of input count rate. Solid line is a linear fit to the data. Data points are labeled by the beam energy at which they were measured.

part of the aperture out of the beam. Therefore, the actual number of beam electrons that enter the detector, when it is at a non-zero angle with respect to the beam, is smaller than would be indicated by the measured monitor detector count rate.

The absolute number of particles incident on the detector depends sensitively on the beam profile which is not accurately known. Qualitative arguments in Section 2.4 will indicate that the beam has roughly constant intensity over most of the beam spot area but drops off sharply near the edges. In the data analysis in this section, the finite size of the beam spot is ignored and the data at all angles are normalized to the monitor count rate. This procedure overestimates the flux into the detector since some of the beam particles seen by the monitor detector may be outside the entrance aperture of the Fluxmeter. The error in absolute normalization is estimated to be 30%.

Normalization to the measured monitor count rate thus underestimates the detector response at larger angles relative to the response at smaller angles. This effect becomes significant for angles greater than  $12^\circ$ . However, the large angle response of the detector is a small contribution to the total response so that the total error introduced by this effect in the angle-integrated geometric factor is small compared to other experimental uncertainties. The large angle response of the Fluxmeter is an important consideration in the calculations of Section 2.4 and it is treated there in more detail.

The quantity of interest in the calibration of the Fluxmeter is the geometric factor as a function of incident electron energy,  $G(E)$ . Geometric factor is defined by

$$G(E) = 2\pi \int_0^{\theta_{\max}} A(E, \theta) \sin(\theta) d\theta \quad (2.2)$$

where  $A(E, \theta)$  is the effective detector area as a function of energy and angle of incidence of the electrons and  $\theta_{\max}$  is the largest angle for which  $A(E, \theta)$  is non-vanishing. If the effective area is defined by two concentric circular apertures, with radii  $r_1$  and  $r_2$  and separated by a distance  $D$ , then  $A(\theta)$  is given by

$$A(\theta) = \begin{cases} r^2 \cos(\theta) & \text{If } 0 < \tan(\theta) < (R - r)/D \\ \cos(\theta) [f(r, R) + f(r, R) - D h(R, r) \tan(\theta)] & \text{If } (R - r)/D < \tan(\theta) < (R + r)/D \\ 0 & \text{If } \tan(\theta) > (R + r)/D \end{cases} \quad (2.3)$$

where  $r$  and  $R$  are the smaller and larger of the values of  $r_1$  and  $r_2$ , respectively, and the functions  $f$  and  $h$  are given by

$$f(x,y) = x^2 \cdot \cos^{-1} \left[ \frac{(x^2 - y^2 + D^2 \tan^2(\theta))}{2 x D \tan(\theta)} \right]$$

and

$$h(x,y) = \left[ \frac{x^2 + y^2}{2} - \frac{(x^2 - y^2)^2}{4 D^2 \tan^2(\theta)} - \frac{D^2 \tan^2(\theta)}{4} \right]^{1/2}$$

Substituting eq. (2.3) into eq. (2.2) and integrating yields

$$G = \frac{\pi^2}{2} \left[ r_1^2 + r_2^2 + D^2 - ((r_1^2 + r_2^2 + D^2)^2 - 4r_1^2 r_2^2)^{1/2} \right] \quad (2.4)$$

Using purely geometric considerations, the opening angle of the Fluxmeter is defined by the entrance collimator ( $r_1 = 0.635$  cm) and the collimator in front of the back solid state detector ( $r_2 = 0.264$  cm). The two collimators are 4.83 cm apart. In this geometry  $\theta_{\max} = 9.3^\circ$  and an evaluation of eq. (2.4) yields  $G(E) = 1.2 \times 10^{-2}$  cm<sup>2</sup>-sr.

The measured  $\theta_{\max}$  and  $G(E)$ , however, are considerably different from those calculated using only geometric considerations. The reason for this deviation is electron multiple scattering in the entrance Be foil and the two solid state detectors. For angles of incidence smaller than  $\theta_{\max}$ , the effect of the scattering is to decrease the number of electrons that reach the BGO crystal as many electrons are scattered away from the detectors and absorbed by the collimators and spacers. On the other hand, electrons with angles of incidence larger than  $\theta_{\max}$ , which would not otherwise reach the BGO crystal, may be scattered into the BGO. The net effect is to greatly reduce the magnitude of the angle integrated quantity,  $G(E)$ , but to increase  $\theta_{\max}$  above the values calculated by ignoring scattering effects. A more thorough discussion of scattering is contained in section 2.4.

The effective detector area,  $A(E, \theta)$ , is determined from the data using

$$A(E, \theta) = \frac{\sum_{i=1}^{i_{\max}} (N_i/10)}{(\text{MON}/\text{DT})} \cdot A_0 \quad (2.5)$$

where  $N_i$  is the number of BGO counts collected during the  $i^{\text{th}}$  10 second data collecting interval ( $i_{\text{max}}$  varied from 3 to 8), MON is the monitor count rate in Hz, DT is the calculated monitor dead time factor and  $A_0$  is the collimated beam spot area,  $1.27 \text{ cm}^2$ . The monitor dead time factor was calculated from the expression

$$DT = 1.02642 - \text{MON} * 0.00337 \quad (2.6)$$

which is the best straight line fit to the measured monitor detector dead time correction factor (Fig. 2.1). The geometric factor,  $G(E)$ , is calculated from the data by using eq. (2.2) with  $A(E, \theta)$  given by the measured values of BGO area at  $0^\circ$ ,  $6^\circ$ ,  $12^\circ$  and  $18^\circ$  for the angular ranges of  $0^\circ$ - $3^\circ$ ,  $3^\circ$ - $9^\circ$ ,  $9^\circ$ - $15^\circ$  and  $15^\circ$ - $21^\circ$ , respectively.

### 2.3 Experimental Results

The nominal operating voltage for the BGO photomultiplier tube (PMT) is the high voltage setting 128. Most of the calibration work was performed at this setting and is discussed first in this section. A discussion of the results with different high voltage settings is at the end of this section.

The sensitivity of the Fluxmeter to electrons with energies below the threshold energy of 1 MeV was investigated using high intensity (monitor count rate was approximately 57 kHz) beams. In the configuration which required both solid state detector signals to be in coincidence with the BGO signal, the Fluxmeter showed no response to electrons while under bombardment by 0.25, 0.50 and 0.75 MeV beams.

The experimentally determined values of  $A(E, \theta)$ , obtained using eq. (2.5), are tabulated in Table 2.1 for the various electron energy channels. Table 2.2 shows the geometric factors derived using the measured  $A(E, \theta)$  values. The data from Table 2.2 are plotted in Fig. 2.2. It is evident that, for the electron energies below 1.75 MeV, the total geometric factor is much smaller than the nominal value of  $1.2 \times 10^{-2} \text{ cm}^2\text{-sr}$  and is rapidly decreasing with decreasing energy. The reason for this is that the effects of multiple scattering and absorption are much larger at lower energies than at higher ones. The 1 MeV electrons are just barely energetic enough to reach the BGO crystal and so are subject to the largest effect. Examination of Fig. 2.2 also shows that measurements with electron beams with energies above 2 MeV are necessary to completely characterize the response of even the lowest electron channel, LL-L1.

Fig. 2.3 shows the ratio of counts in the LL-L1 channel to the total number of counts in all channels as a function of angle of incidence for 1.50 and 1.75 MeV electrons. Evidently, this ratio is constant for all angles of interest, which implies that the size of the signal from the BGO crystal is independent of bombarding angle in the  $0^\circ$  to  $18^\circ$  range. This effect can be understood by considering the geometry of the Fluxmeter. The

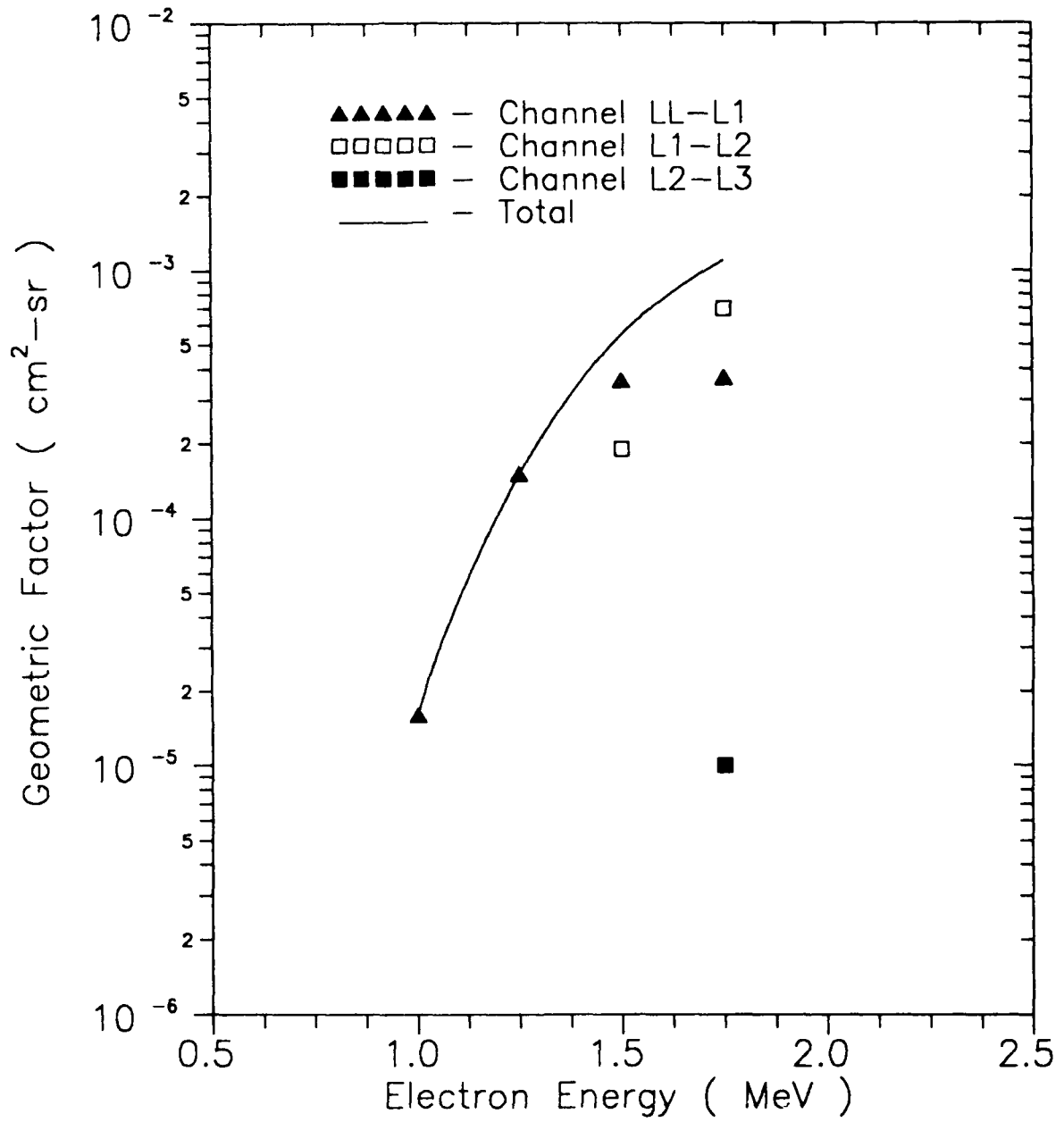


Figure 2.2 Geometric factor as a function of electron energy for the first three electron channels and their sum. Solid line is drawn through the sum points to guide the eye.

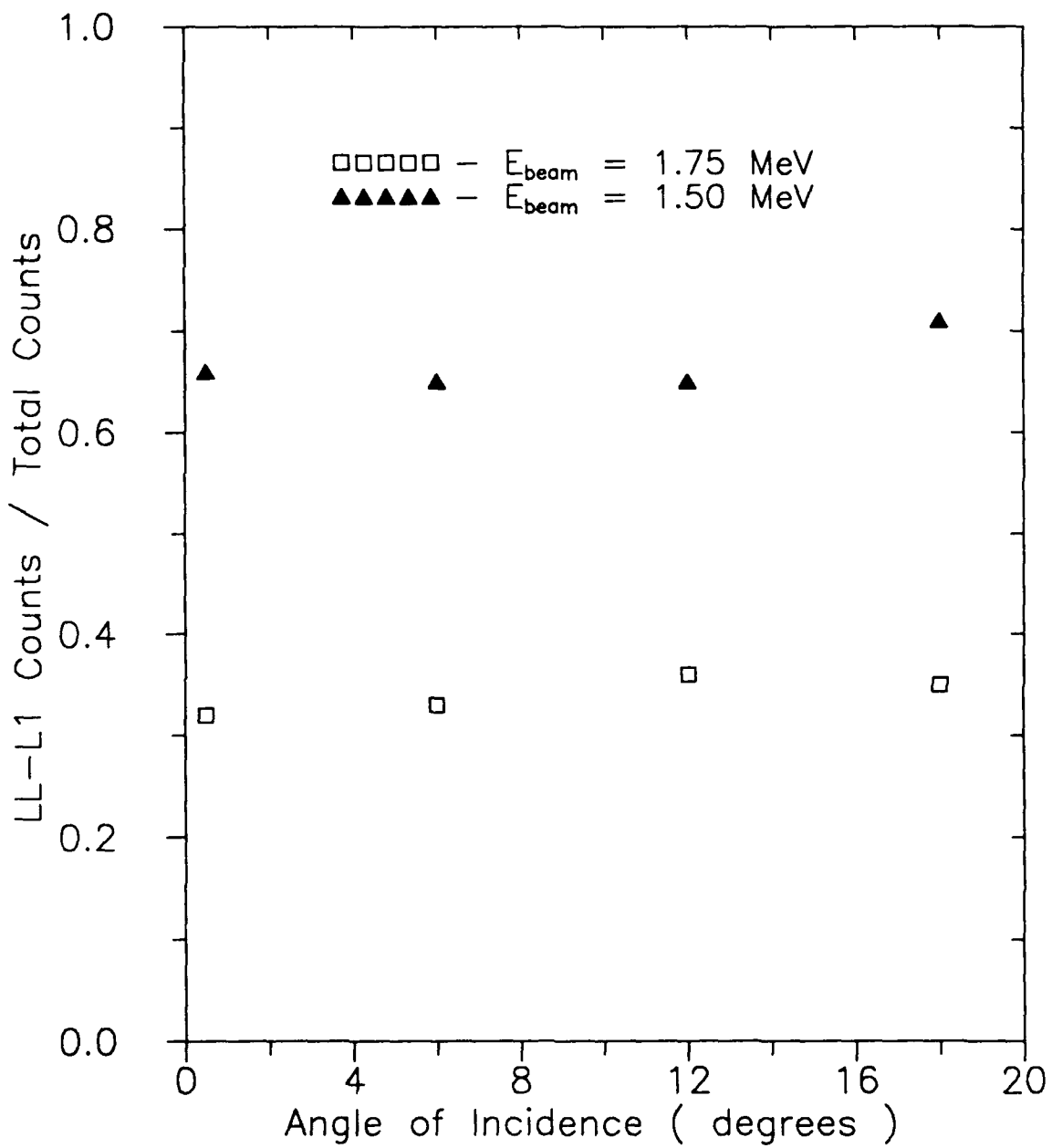


Figure 2.3 Ratio of LL-L1 channel counts to the sum of counts in the LL-L1 and L1-L2 channels.

Table 2.1

Effective area of the three lowest Fluxmeter BGO channels as a function of electron energy. Area is in units of  $10^{-4}$  cm<sup>2</sup>.

Channel	Energy (MeV)	Angle of Incidence (degrees)						
		0.0	3	6	9	12	15	18
LL-L1	1.00	0.8	—	1.0	—	0.5	—	0.2
	1.25	15.7	14.0	12.8	8.3	4.6	1.0	0.1
	1.50	27.6	—	25.9	—	11.4	—	0.3
	1.75	19.5	—	21.0	—	13.4	—	1.2
LL-L2	1.50	13.0	—	12.8	—	6.5	—	0.2
	1.75	38.0	—	38.3	—	25.2	—	3.1
LL-L3	1.75	0.5	—	0.5	—	0.4	—	0.0

Table 2.2

Geometric factors for the three lowest Fluxmeter electron channels. Units are  $10^{-5}$  cm<sup>2</sup>-sr.

Channel	Electron Energy (MeV)			
	1.00	1.25	1.50	1.75
LL-L1	1.85	15.5	36.4	36.9
L1-L2	0.0	0.0	19.2	70.4
L2-L3	0.0	0.0	0.0	0.9
TOTAL	1.85	15.5	55.6	108.2

collimation in the Fluxmeter is very tight so that only electrons moving on trajectories nearly perpendicular to the back solid state detector can enter the BGO crystal. Therefore, the angular distribution of trajectories and, consequently, the energy deposition of electrons that enter the BGO is, to a good approximation, a function of the electron energy only, and not of the initial angle of incidence.

Although HV-128 is the nominal setting for the PMT, the Fluxmeter response was measured for a range of HV settings, from HV-0 to HV-255. If the operating voltage of the PMT needs to be changed from the HV-128 setting, the results of the high voltage sweep measurements allow the calculation of appropriate corrections to the HV-128 calibration. In addition, these measurements can be used to determine the efficiency of counting electrons as a function of their energy.

Fig. 2.4 shows the count rate (relative to that at HV-128) at  $0^\circ$  for 1.0 and 1.5 MeV electrons for a variety of high voltage settings. The count rate for 1.5 MeV electrons is a very slowly rising function of the high voltage above HV-100. This indicates that above this setting the detection efficiency is near its maximum level and raising the voltage, or lowering it slightly, will not change it very much. On the other hand, the relative count rate for 1.0 MeV electrons rises steeply with increasing voltage above HV-128 and only appears to level off above HV-255. Consequently, a change in the high voltage setting, from HV-128, will change the detection efficiency for 1.0 MeV electrons. This change is due to the fact that average energy deposited in the BGO crystal by a 1.0 MeV electron is near the detection threshold and an increase in the amplification, effected by raising the high voltage, makes the PMT signals larger. Consequently, more of the previously sub-threshold signals are raised above the detection threshold thus increasing the detection efficiency.

The change in signal size as a function of applied PMT voltage is apparent from Fig. 2.5. All the data points were taken with a 1.5 MeV beam so that the amount of energy deposited in the BGO crystal remained constant. As the voltage was increased, counts were taken out of the lowest LL-L1 channel and appeared in the higher L1-L2 and L2-L3 channels.

## 2.4 Theoretical Analysis of the Fluxmeter Electron Response

### 2.4.1 Description of Fluxmeter Model

As is evident from the discussion in Section 2.3, the performance of the Fluxmeter deviates significantly from the predictions based on the detector geometry alone. Therefore, a model of the interaction of the detector with incident electrons has been developed to verify that the response of the Fluxmeter can be understood if the effects of multiple scattering and beam spot geometry are properly taken into account. The model will be described in this section while the comparison of the model calculations with the data will be shown in Section 2.4.2.

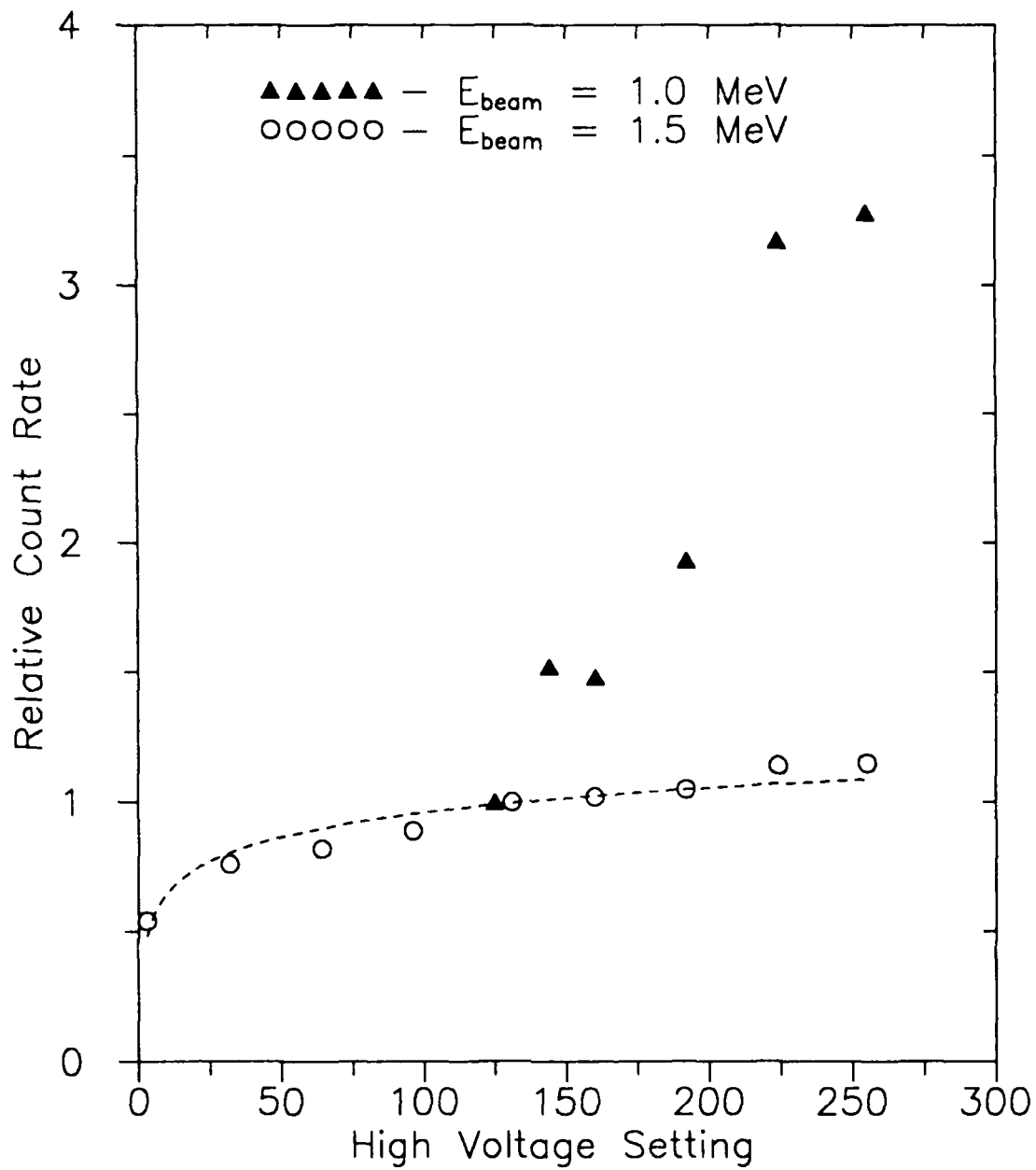


Figure 2.4 Count rate at  $0^\circ$  relative to the count rate with HV-128. Dashed line is a smooth curve drawn through the 1.5 MeV data points.

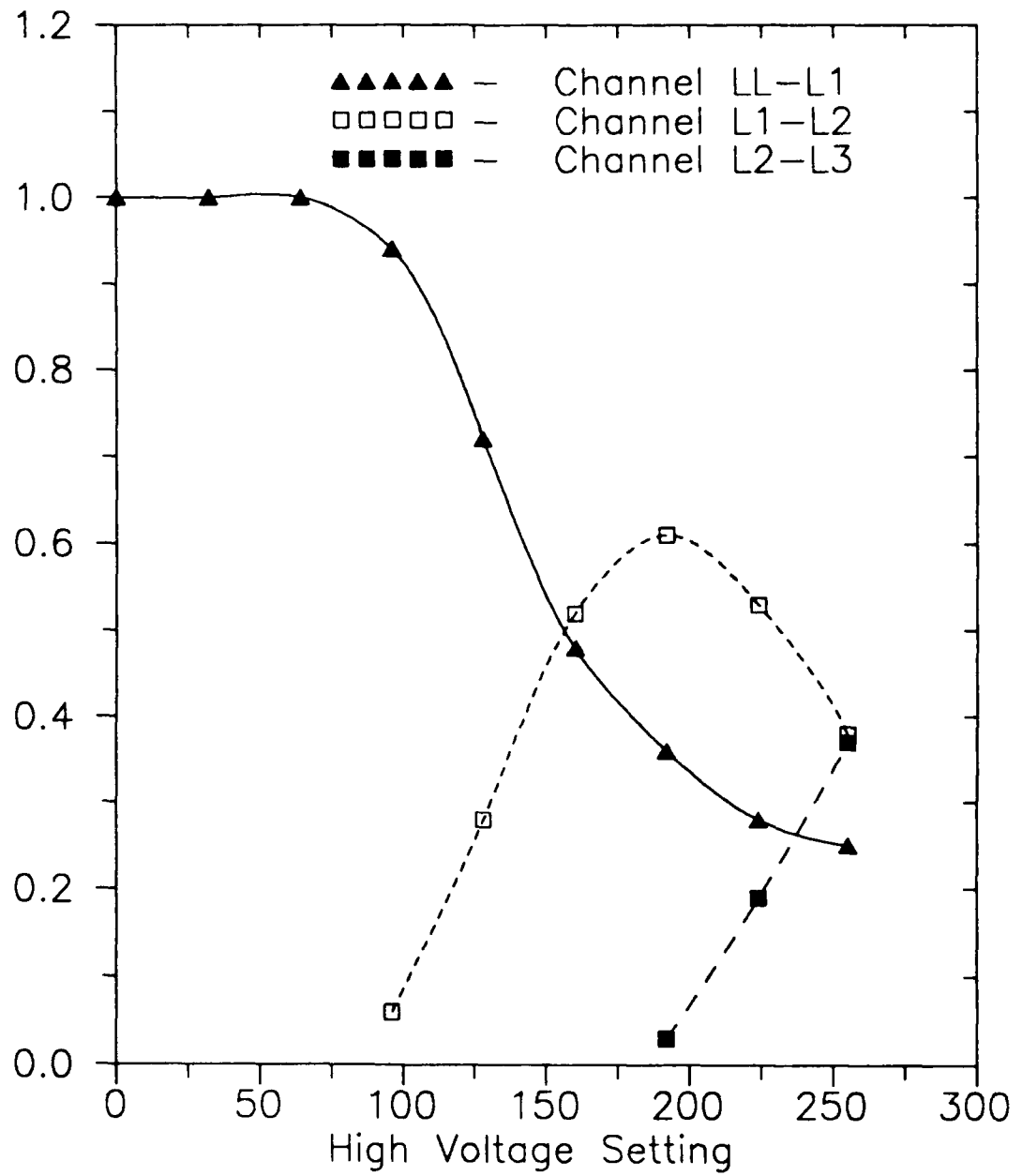


Figure 2.5 Fraction of the total Fluxmeter counts that are recorded in a given electron channel. Curves are cubic splines drawn to guide the eye.

The Fluxmeter is represented in the model as a set of apertures. The first aperture is the tungsten entrance collimator of the Fluxmeter, the last is the opening in the aluminum detector holder of the back SSD just before the BGO scintillator. The various apertures and their positions and physical dimensions are shown in Table 2.3. As the electron moves through the Fluxmeter toward the BGO it must pass inside every aperture. Those electrons whose trajectories fall outside an aperture are assumed to be absorbed and fail to reach the BGO. At three of the apertures ( Be foil, SSD-Front and SSD-Back ) the electron suffers multiple scattering, with the angular distribution given as described below.

The multiple scattering angular distributions were obtained using the results of a study by Seltzer and Berger (Ref. 2.1). These authors measured electron scattering distributions and found that in a energy range between 0.1 and 0.4 MeV the distributions depend to first order only on the parameter  $z/r_0$ , the ratio of the target thickness,  $z$ , to the total range of the electron in the target material,  $r_0$ . An assumption was made that this parameter dependence can be extended to the energy range of interest of the Fluxmeter. The range and energy loss of electrons in various materials was calculated from the tables of Ref. 2.2.

The Be entrance foil has a thickness of 6 mils so that for 1.5 MeV electrons  $z/r_0 = 0.03$ . Interpolation from Ref. 2.1 gives the angular distribution as a near Gaussian shape with the standard deviation of approximately  $14^\circ$ . The distributions for scattering from silicon (the material of the SSD's) were not available in the literature and the following procedure was adopted to estimate them. An angular distribution,  $f_0(\theta)$ , for the proper value of  $z/r_0$ , was interpolated from the data of Rester and Derrickson (Ref. 2.3), who measured the scattering of 1 MeV electrons from aluminum foils.

Since aluminum and silicon differ only slightly in mass and electron number it is reasonable to assume that their electron multiple scattering distributions for energetic electrons will be similar. In the model calculations  $f_0(\theta)$  as well as two other related distributions,  $f_1(\theta) = f_0(1.2 \cdot \theta)$  and  $f_2(\theta) = f_0(1.5 \cdot \theta)$ , were used. The three distributions are shown in Fig. 2.6. Best results were obtained with  $f_2$  and all calculation results quoted in this report use that distribution. In view of the uncertainties in determining the silicon angular distributions, it is felt that the use of  $f_2$  is justified.

A small correction for the probability of reflection of an electron from the 700 micron thick SSD was also made. Extrapolation from the data of Ref. 2.1 for aluminum gives the reflection probability of approximately 4.5% at each solid state detector. No correction was made for the electron reflection probability from the BGO as no such data were available. However, this probability must be larger than the reflection probability from the thinner SSD's, so that the calculated BGO count rate is too high by at least 5%.

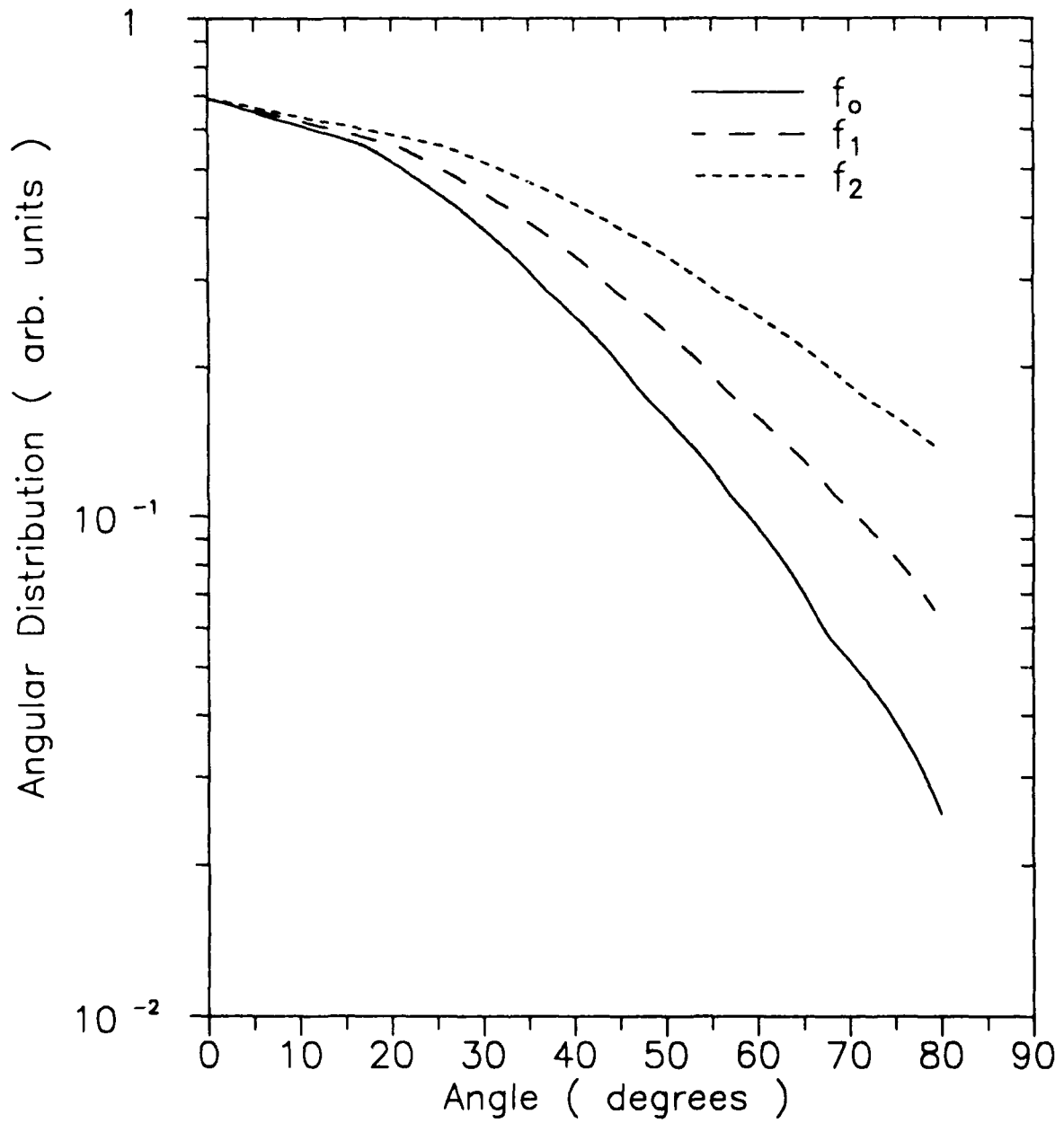


Figure 2.6 Angular distributions from electron multiple scattering.  $f_0$  is extrapolated from data of Ref. 2.3.,  $f_1$  and  $f_2$  are defined in the text.

TABLE 2.3

Listing of Apertures and Aperture Parameters  
Used in the Fluxmeter Simulation Calculation.

Aperture	Description	Distance ( cm )	Radius ( cm )
1	Entrance Collim. (Front)	0.00	0.64
2	Entrance Collim. (Back)	0.51	0.64
3	SSD-F Collim. (Front)	1.78	0.48
4	SSD-F Collim. (Back) (Be Foil)	2.29	0.48
5	SSD-F Detector	2.67	0.56
6	SSD-F Holder (Back)	3.05	0.60
7	SSD-B Collim. (Front)	4.32	0.26
8	SSD-B Collim. (Back)	4.83	0.26
9	SSD-B Detector	5.21	0.40
10	SSD-B Holder (Back)	5.59	0.46
11	BGO Crystal	5.67	1.27

Note: Numbers in distance column indicate distance  
from the front of the entrance aperture.

The solid state detector electron detection efficiency has been measured for detectors with only a small, central portion of the active area exposed. The efficiency of detection of electrons over the entire surface of the detector is not well known and, in fact, may vary from detector to detector. The reason for this is that the energy deposited in an SSD by an electron is small and charge collection efficiency close to the edges of the detector depends on the manufacturing details of the SSD as well as the applied bias voltage. An attempt was made to account for the relatively poor charge collection near the detector edge by requiring that the entire electron track must be contained inside the SSD. In cases where the electron exited the detector through the side, rather than the back, it was assumed that the electron was not detected by the SSD.

During the calibration work at GSFC a number of measurements were taken of the BGO scintillator count rate with both triple coincidence requirement (BGO - SSD-Front - SSD-Back) and double coincidence requirement (BGO - SSD-Front or BGO - SSD-Back). The ratios of the count rates are plotted in Fig. 2.7. Evidently the triples rate is approximately 80% of the doubles rate regardless of electron energy, angle of incidence and of which SSD is used in the double coincidence. This suggests that, for the electron energy range studied, there exists an inefficiency in the electronics for detection of BGO - SSD coincidences. Such an effect may be due to timing jitter of the signals from the various detectors sometimes exceeding the required coincidence overlap time. Accordingly, the calculated BGO count rate was multiplied by a factor of 0.64 (i.e.  $0.8 \times 0.8$ ) when compared to the triple coincidence data.

The exact beam spot geometry was not well known, as was discussed in Section 2.2. Therefore, several beam spot geometries were tried in the model calculations. Initially the calculations were performed assuming a beam uniform across the Fluxmeter entrance aperture. In view of the fact that the beam spot is finite in size and that the rotation of the Fluxmeter moved the entrance aperture partly out of the beam, this geometry is unrealistic. Two other shapes of beam spots were used. Both are Gaussian shapes, centered on the Fluxmeter symmetry axis when the Fluxmeter is at  $0^\circ$ , one with a standard deviation,  $\sigma$ , of 0.7 cm and the other with  $\sigma = 0.5$  cm. The first one is rather flat across the detector entrance with a gradual fall off, the second one is sharply peaked at the center with a much steeper fall off toward the edges. As will be evident from the analysis of the next section, the actual shape of the beam spot was probably intermediate between the two, flat over most of the area but with a rapid fall off near the edges.

#### 2.4.2 Model Calculations and Comparison With Data

The actual model calculations were carried out by a Monte Carlo computer code, FLUX\_M5, written in the Turbo Pascal programming language for the IBM PC. Electron tracks were generated at the entrance aperture of the Fluxmeter with a fixed

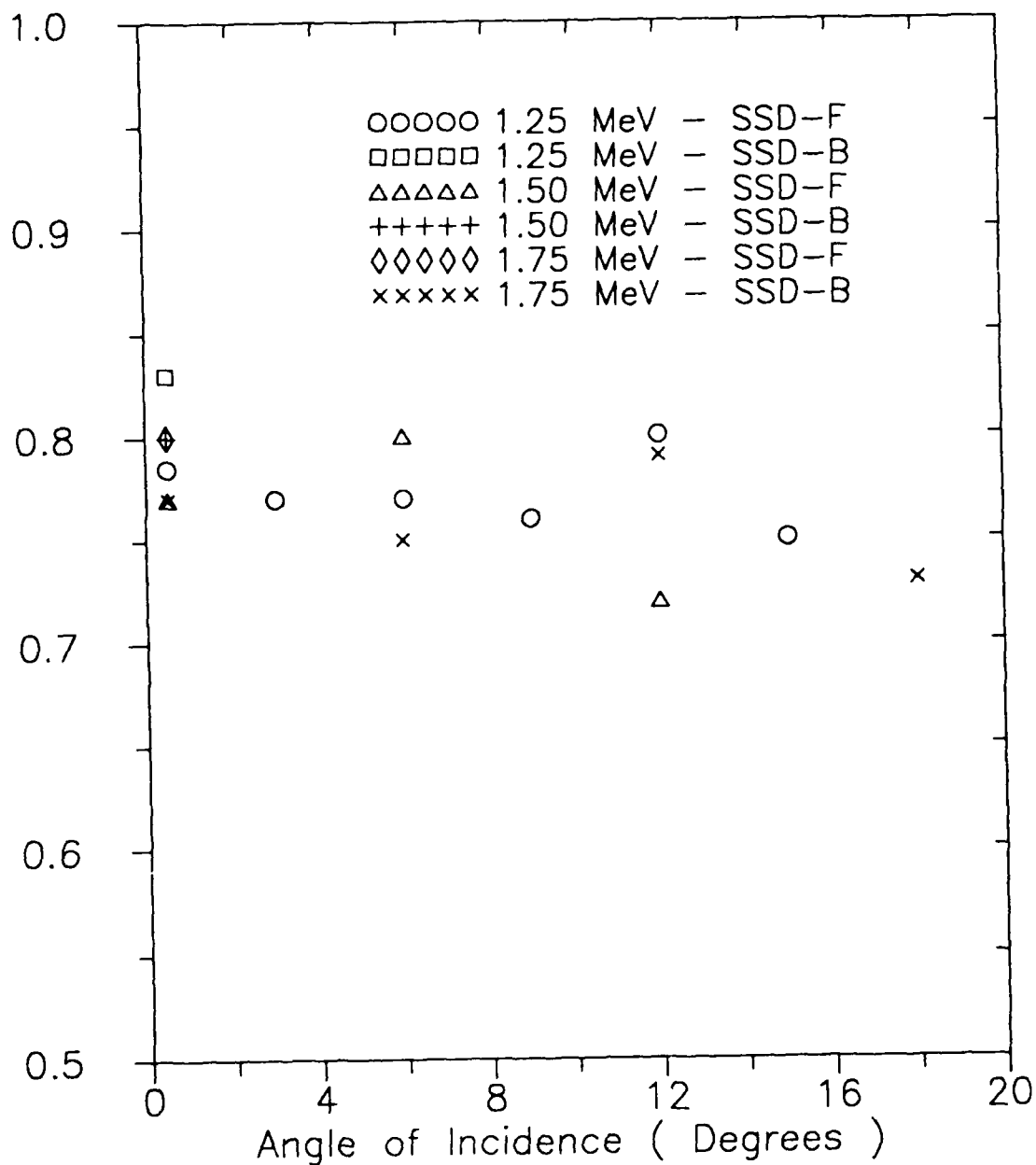


Figure 2.7 Ratio of triple coincidence counts to double coincidence counts. Legend indicates which SSD is required in the double coincidence.

angle of incidence and initial positions given by the Gaussian beam spot distribution functions of Section 2.4.1. Each track was followed through the Fluxmeter for as long as it fit inside the successive apertures listed in Table 2.3. Once the track passed outside an aperture, the calculation for that event was stopped. At the Be foil and the two solid state detectors the angle of the track was altered by folding the pre-scattering track angle with the multiple scattering angle. The multiple scattering angle was chosen randomly using the  $f_2(\theta)$  distribution function described in the previous section.

For each initial electron incidence angle, 10,000 events were generated at the Fluxmeter entrance aperture and their tracks followed until they either reached the BGO crystal or were removed from calculation. The output of the program was the number of electrons detected by the front SSD, the back SSD, and the BGO scintillator. Due to the difficulty in obtaining proper multiple scattering distributions, the calculations were only carried out for 1.5 MeV electrons.

The model calculations of the effective area of SSD-Front and the values extracted from the data are shown in Fig. 2.8. For angles of incidence up to  $12^\circ$  the data are well reproduced by the calculation with the beam spot width parameter,  $\sigma$ , of 0.7 cm. At the largest angle,  $18^\circ$ , the calculation with  $\sigma = 0.5$  cm provides a much better fit to the data. This is evidence for a beam intensity uniform over much of the Fluxmeter with a rapid fall off in intensity near the edges.

The calculated and measured values of the geometric factor of SSD-Back are shown in Fig. 2.9. Once again, it is evident that the data for angles up to  $12^\circ$  are better reproduced by a uniform beam intensity over the central region of the detector. The large angle data indicate a rapid intensity fall off near the edges of the beam spot. Finally, the experimental and theoretical geometric factors of the BGO scintillator are shown in Fig. 2.10.

Given the uncertainties in some of the model parameters, the calculations reproduce the data quite well. The calculations provide a reasonable fit to the BGO count rate data for all except the largest angles and even there the general trend of the data is reproduced. The experimental counting statistics and the calculation's uncertainties are the greatest at  $18^\circ$ , so that good absolute agreement between data and theory cannot be expected at this large angle.

### 3. HIGH ENERGY ELECTRON RESPONSE

The response of the Fluxmeter to electrons with energies between 1.3 and 10.8 MeV was measured at the Rome Air Development Center (RADC) LINAC at Hanscom Air Force Base. The experiment, analysis of the collected data, and final results are discussed in this Section.

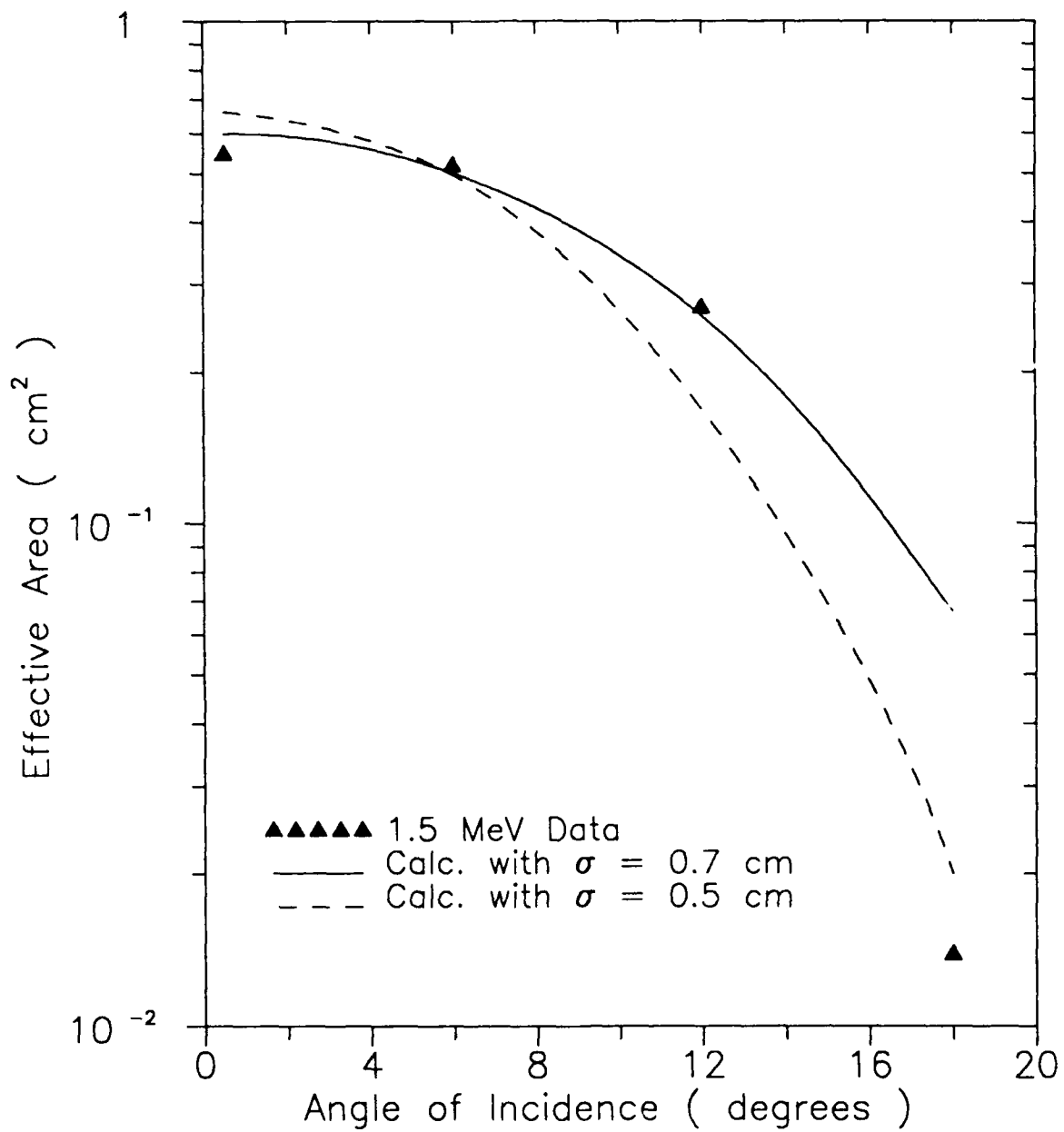


Figure 2.8 Effective area of SSD-Front.

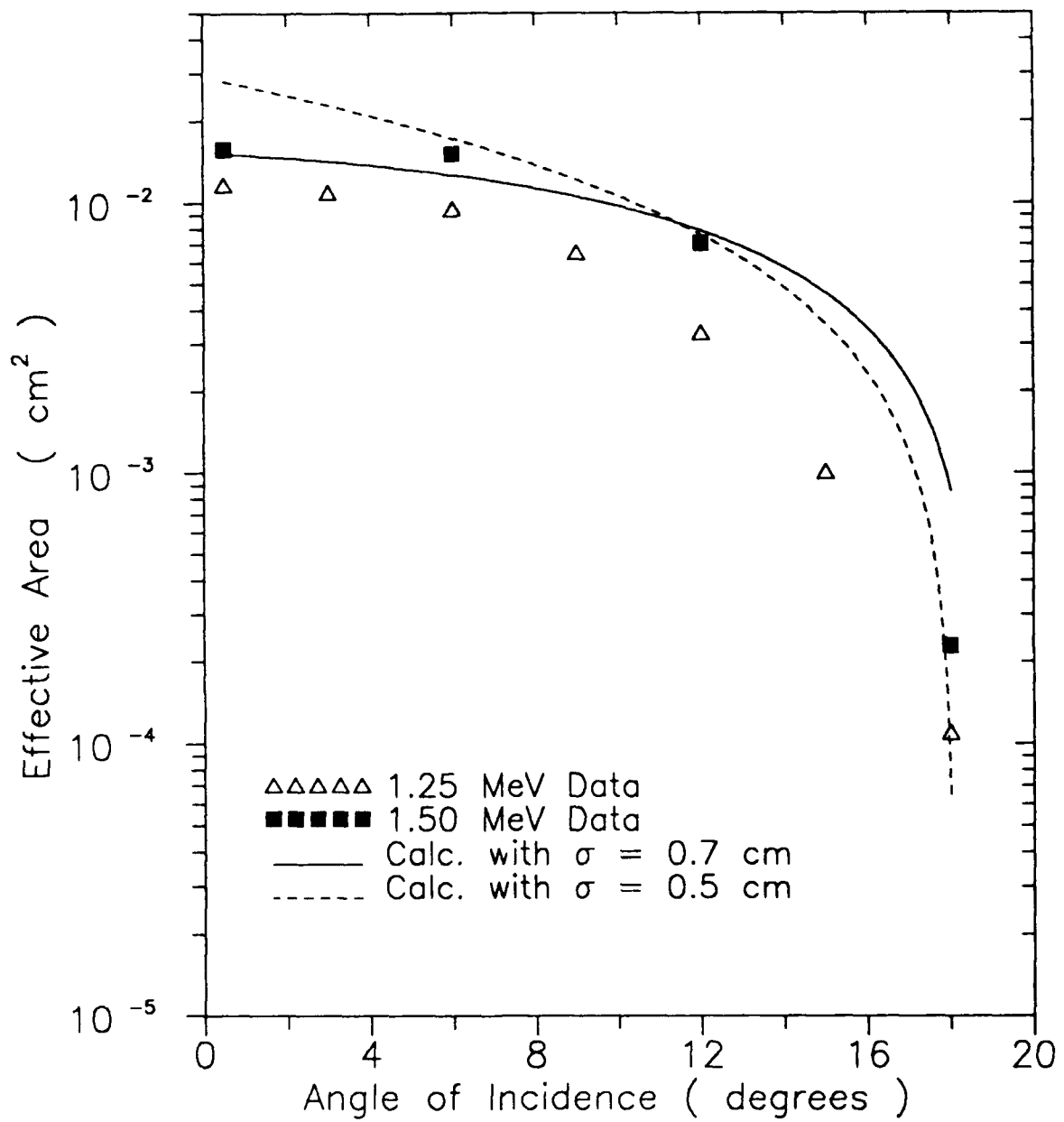


Figure 2.9 Effective area of SSD-Back.

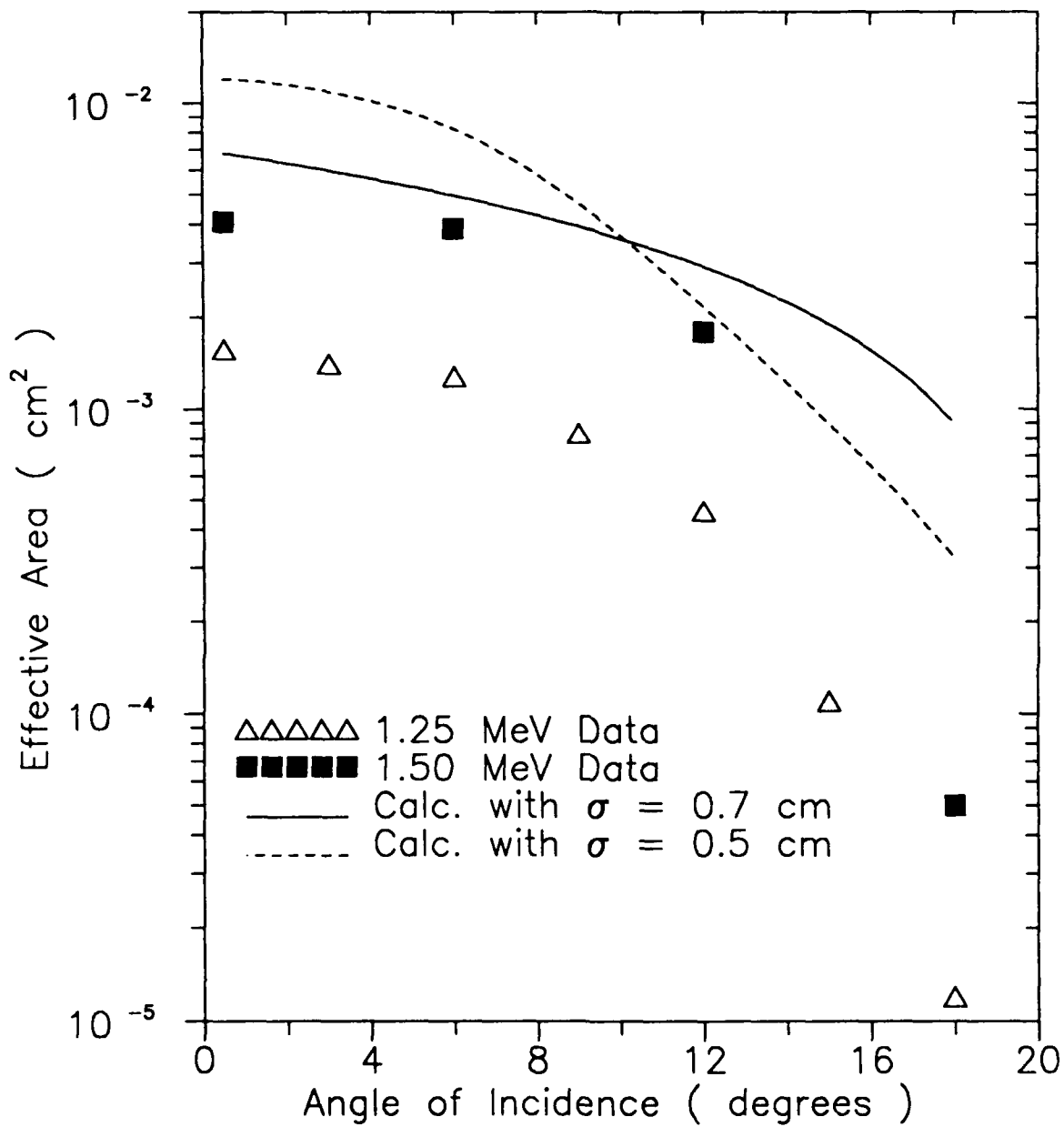


Figure 2.10 Effective area of the BGO scintillator.

### 3.1 Experimental Arrangement

The Fluxmeter was mounted on a rotating table at a distance of approximately 1.2 meters from the flange at the end of the 30° LINAC beam line. Beam electrons had to travel through the flange, consisting of aluminum and cooling water, and the 1.2 m air gap before striking the Fluxmeter. The total amount of degrader areal density was equivalent to 0.61 gm/cm<sup>2</sup> of water. A 1500 μm solid state beam monitor detector was mounted near the Fluxmeter. This detector had a 1.27 cm thick lead collimator with a 0.47 cm diameter hole and its center was 10 cm from the central axis of the Fluxmeter (also the beam axis).

The monitor detector did not move when the Fluxmeter was rotated with respect to the beam. Therefore, it was used to provide the relative angle-to-angle normalization as the Fluxmeter response was mapped out as a function of angle at a fixed beam energy. The fact that the monitor was located 10 cm from the Fluxmeter axis made it unsuitable for use in determining the absolute beam normalization at the Fluxmeter location. The absolute beam normalization was provided by the SSD-Front detector when the Fluxmeter was at 0° with respect to the beam.

The energy loss of the beam electrons in the degrader material was obtained using the data from Berger and Seltzer. (Ref. 2.2). Table 3.1 lists the nominal beam energies, the effective beam energies after the degrader and the angular ranges that were studied with the RADC LINAC beam. Multiple scattering, suffered by the beam electrons in the degrader material, had the effect of spreading the beam out both in angle and energy. Angular beam spreading and its effects are described in Section 3.2 while the energy straggling and its effects are described in Section 3.3.

### 3.2 Angular Distributions

Electron scattering that affects the Fluxmeter has two contributions, external and intrinsic scattering. External scattering is, in principle, under the experimenter's control. It includes the effect of degrader material, if any, that is located between the end of the evacuated beam line and the Fluxmeter. At the GSFC Van De Graaff, for example, the Fluxmeter was in a vacuum chamber so that there was no external scattering. At the RADC LINAC there was a considerable amount of material that the electrons had to traverse before striking the Fluxmeter. Intrinsic scattering is the scattering that takes place in the elements of the Fluxmeter itself, the Be foil and the two solid state detectors. It is fundamental to the design of the detector and part of the true detector response.

The primary effect of external angular scattering on the Fluxmeter calibration data is to distort the angular response of the detector. Electrons moving parallel to the beam axis cannot travel all the way to the BGO crystal through the two solid state detectors once the Fluxmeter has been rotated by more than 15°

Table 3.1

List of energies and angles investigated at the RADC linac.

Nominal Beam Energy (MeV)	Effective Beam Energy (MeV)*	Angles of Measurement (degrees)
2.5	1.3	0, 6, 12, 18, 24
3.0	1.8	0, 6, 12, 18, 24
4.0	2.8	0, 6, 12, 18, 24
4.5	3.3	0, 6, 12, 18, 24
5.4	4.2	0, 6, 12, 18, 24
8.0	6.8	0, 3, 6, 9, 12, 15, 18, 21, 24
10.0	8.8	0, 6, 12, 18, 24
12.0	10.8	0, 6, 12, 18, 24

\* - Energy after traversing the beam pipe flange and air gap

with respect to the beam (see Fig. 2.10). However, electrons which have undergone scattering in the degrader and are moving at some non-zero angle with respect to the beam can still trigger a triple coincidence (SSD-Front, SSD-Back and BGO) for Fluxmeter rotation angles considerably larger than  $15^\circ$ .

The effects of angular scattering are illustrated in Fig. 3.1. The solid line is the limiting Fluxmeter response, calculated using the code FLUX\_M5 assuming no electron scattering. Data taken at 1.25 MeV beam energy at GSFC demonstrate the effects of intrinsic scattering. The intrinsic scattering of 3.5 MeV electrons is less than that of 1.25 MeV electrons, so that the 3.5 MeV RADC data should lie along a curve which shows even less of a scattering effect than the 1.25 MeV data. It is evident that the external scattering suffered by the 3.5 MeV beam at the RADC LINAC distorts the angular distribution to the point that it can no longer be used to calculate the angular response of the Fluxmeter. Electrons with 12 MeV of energy are much less affected by angular scattering effects, both intrinsic and external.

### 3.3 Energy Distributions

Energy straggling is another effect of electron scattering in matter. After traversing some distance in a material, initially mono-energetic beam electrons emerge with a variety of energies clustered around a lower average beam energy. Energy straggling in the Be foil and the two solid state detectors is an intrinsic part of the response of the Fluxmeter, while the straggling of the RADC LINAC beam in the degrader material is an external effect.

The Be foil is much thinner than the solid state detectors so that the intrinsic energy straggling is, to an excellent approximation, equal to the straggling in the  $1400 \mu\text{m}$  of silicon (thickness of SSD-Front plus SSD-Back). Berger et al. (Ref. 3.1) have measured the energy straggling in silicon of electrons with energies between 0.25 and 5 MeV. These authors concluded that the straggling distribution is only a function of the parameter  $z/r_0$  where  $z$  is the material thickness and  $r_0$  is the range of an electron of a given energy. The shape of the straggling distribution, in the range of interest of the parameter  $z/r_0$ , is well approximated by a two sided Gaussian curve

$$S(E) = \begin{cases} (1/\sqrt{2\pi}\sigma_a) \exp(-(E-E_0)^2/2\sigma_a^2) & \text{if } E \leq E_0 \\ (1/\sqrt{2\pi}\sigma_b) \exp(-(E-E_0)^2/2\sigma_b^2) & \text{if } E > E_0 \end{cases} \quad (3.1)$$

where  $\sigma_a$  and  $\sigma_b$  are the standard deviations on either side of the peak of the curve,  $E_0$ . Figs. 3.2 and 3.3 show the  $\sigma_a/E_0$  and  $\sigma_b/E_0$  values, as a function of  $z/r_0$ , taken from Ref. 3.1. The polynomial fits to these values are given by

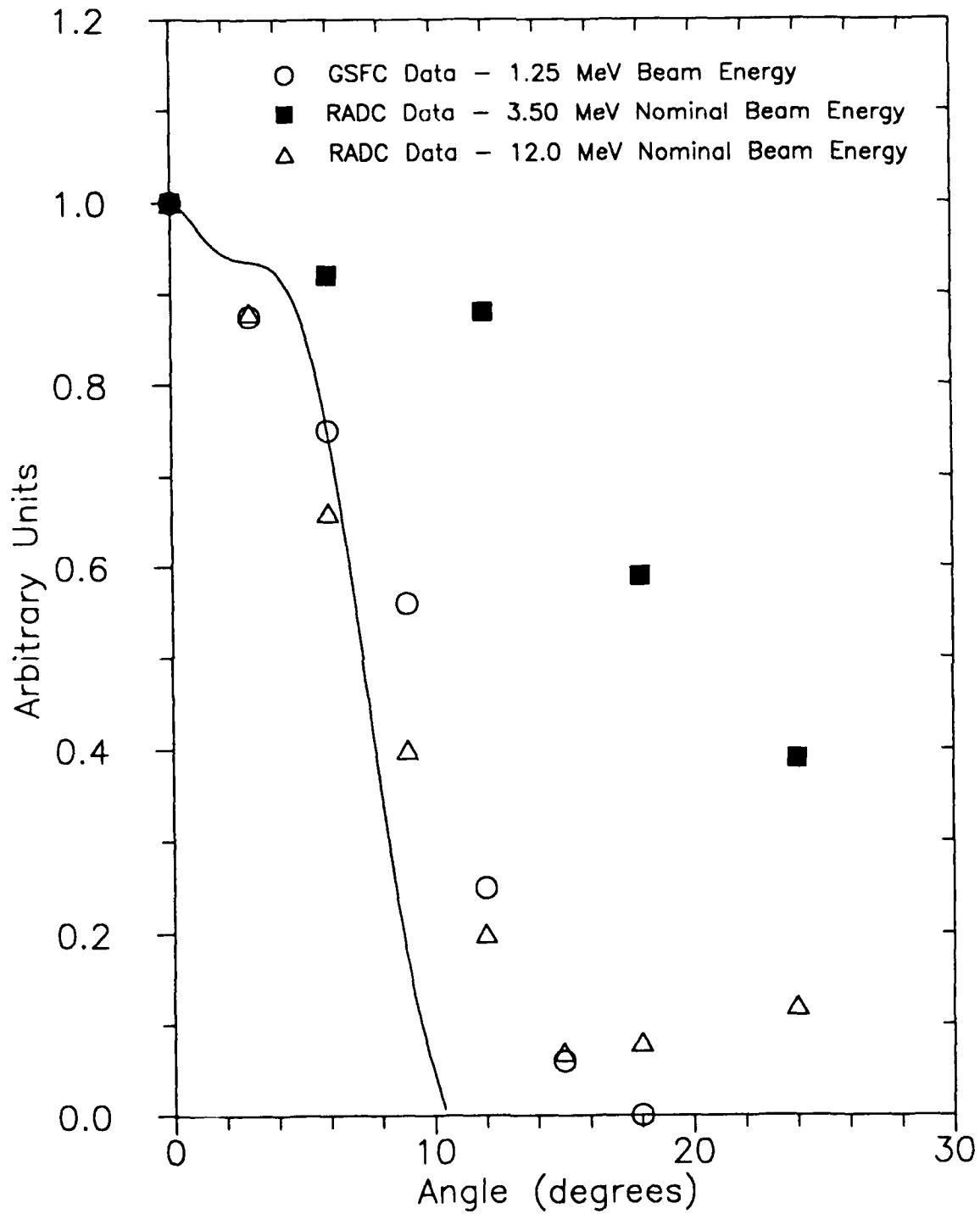


Figure 3.1 Measured angular distributions at RADC and GSFC. Solid line is a curve calculated assuming no electron scattering. All distributions are normalized to unity at zero degrees.

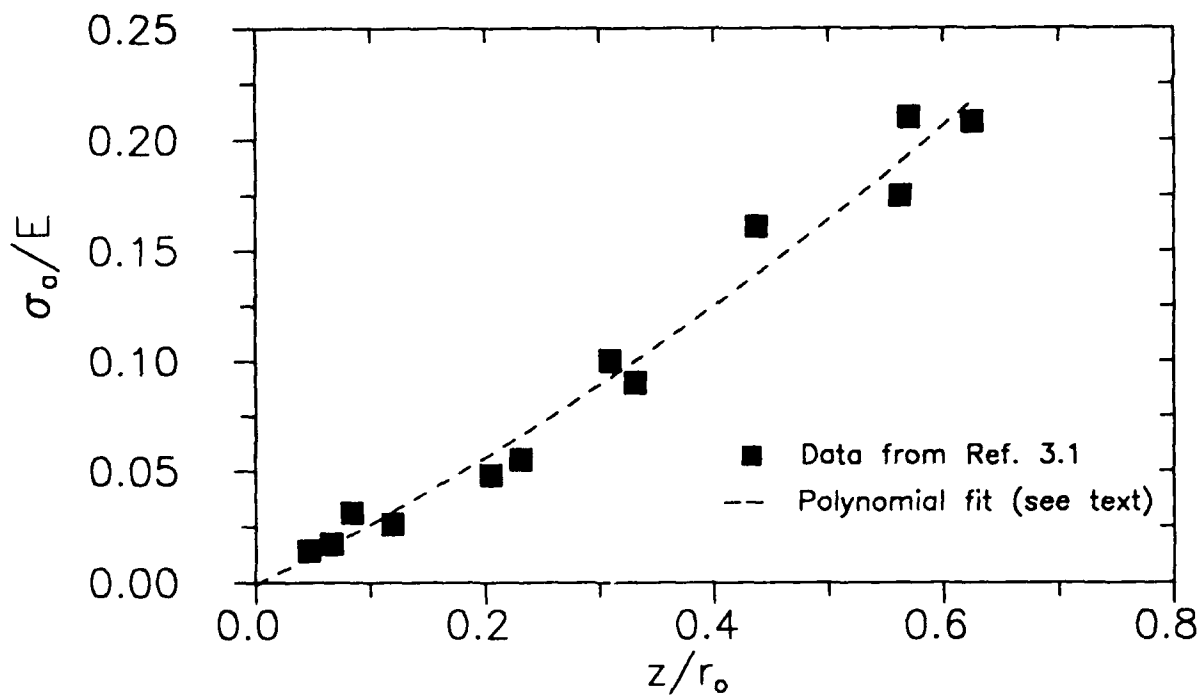


Figure 3.2 Standard deviation  $\sigma_a$  used in eq. (3.1).

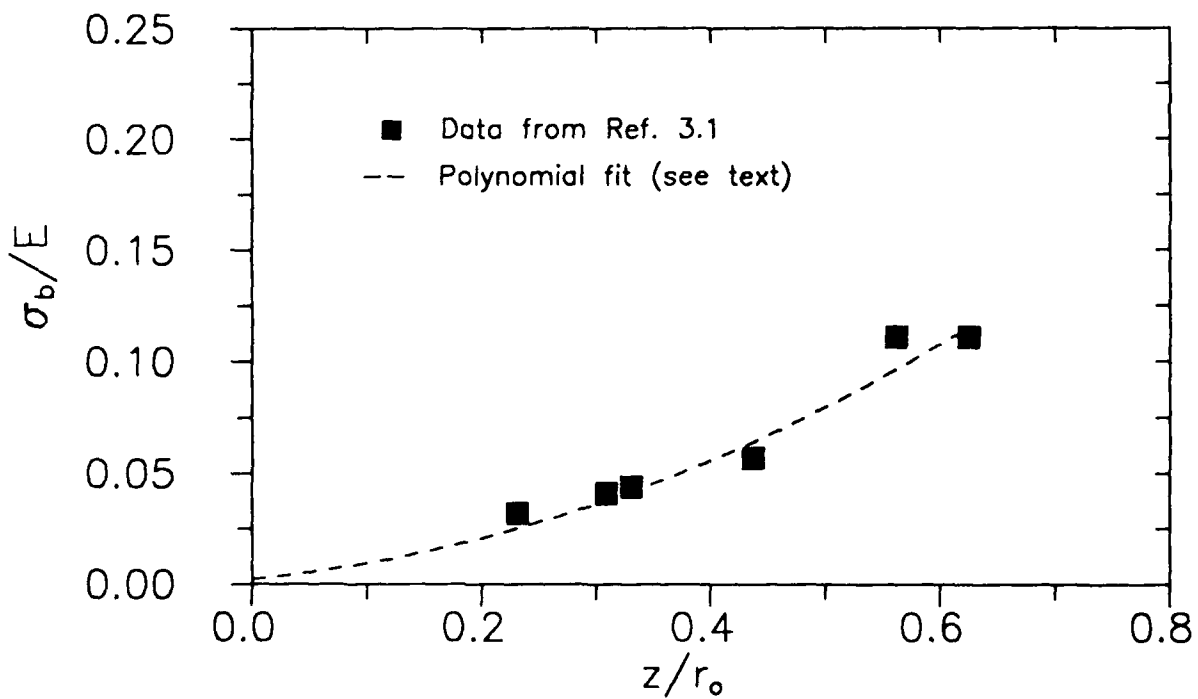


Figure 3.3 Standard deviation  $\sigma_b$  used in eq. (3.1).

$$\sigma_a/E_0 = -0.00174 + 0.25957(z/r_0) + 0.14491(z/r_0)^2 \quad (3.2)$$

and

$$\sigma_b/E_0 = -0.00105 + 0.07230(z/r_0) + 0.18143(z/r_0)^2 \quad (3.3)$$

In the energy range from 0.5 to 10.0 MeV the range of electrons in silicon as a function of energy can be parametrized by

$$r_0(E) = -0.368 + 2.731E - 0.021E^2 \quad (3.4)$$

where E is in MeV and  $r_0$  in mm.

The BGO crystal energy resolution adds another uncertainty to the Fluxmeter energy measurement. An ideal BGO scintillator detection system would have the fractional energy resolution  $dE/E$  proportional to  $E^{-1/2}$ , since the ideal resolution is determined by the counting statistics of the scintillation photons. The actual resolution was determined by fitting the data of Ref. 3.2 and 3.3 with the result that the standard deviation of the resolution function,  $\sigma_{BGO}$ , is given by

$$\sigma_{BGO} = 0.055 \cdot E^{+0.38} \quad (3.5)$$

where E is in MeV.

Fig. 3.4 shows the measured and calculated Fluxmeter pulse height distributions for a 3 MeV RADC linac beam. The experimental spectrum was determined from a pulse height analysis of the buffered output of the photomultiplier tube coupled to the BGO crystal. The calculated spectrum was obtained by folding the BGO resolution function with the effective beam energy distribution. The beam energy distribution was the  $z/r_0 = 0.625$  curve from Ref. 3.1, since the approximate value of  $z/r_0$  for the degrader plus the solid state detectors is 0.61. The agreement between the data and calculated values is quite good, indicating that the Fluxmeter energy response is well understood theoretically.

### 3.4 Data Reduction

Fluxmeter data was collected in ten second intervals, and eight such intervals constituted a data record. Typically, five data records were taken at each energy and Fluxmeter angle setting, one for each of five coincidence modes. The five modes were ON/ON/ON, OFF/ON/ON, ON/OFF/ON, ON/ON/OFF and OFF/OFF/OFF, where the first word indicates the status of the SSD-Front - BGO coincidence, the second word the SSD-Back - BGO coincidence and the last word the plastic scintillator shield - BGO anti-coincidence. The results reported in this section include only data taken with the Fluxmeter in the ON/ON/ON state.

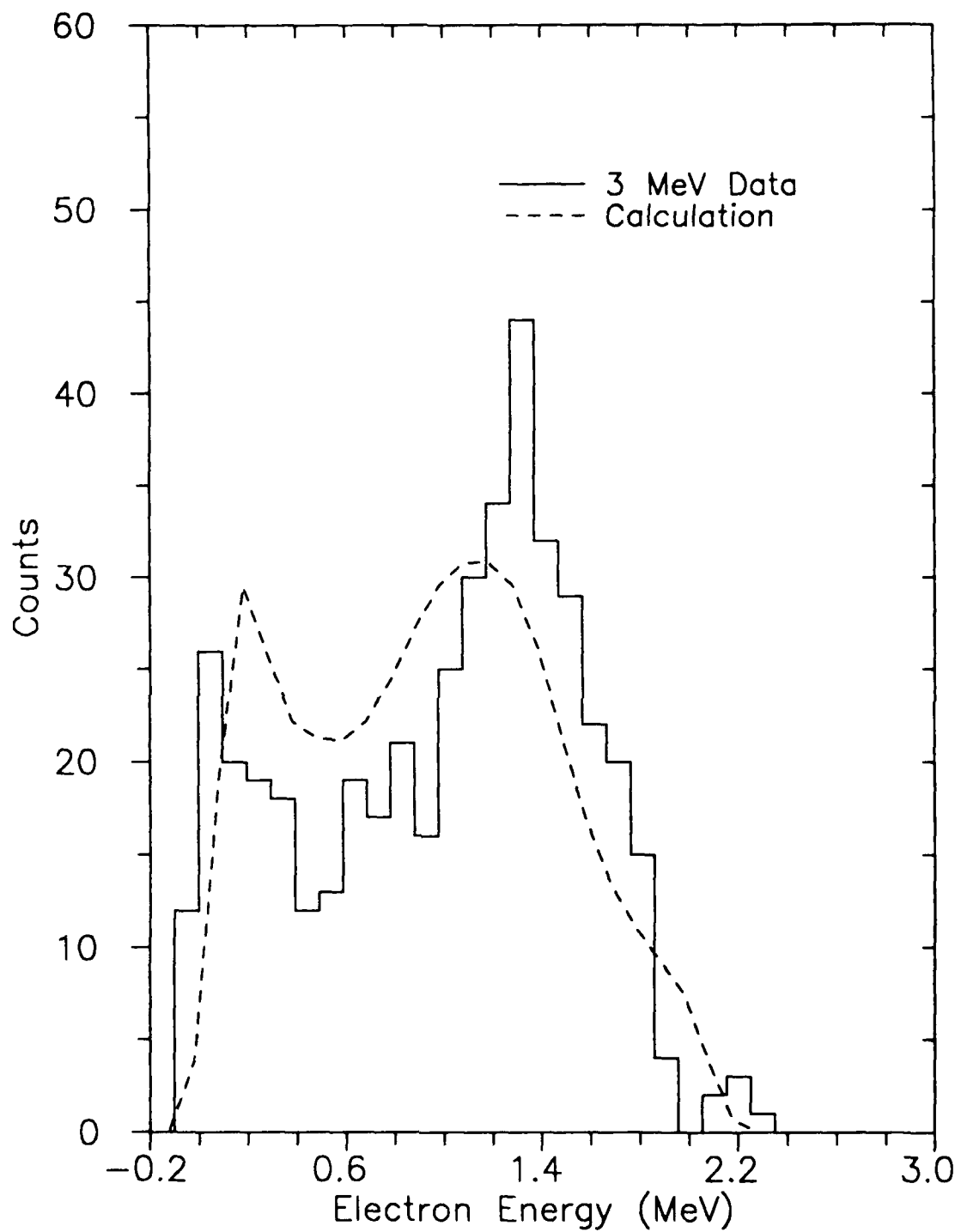


Figure 3.4 Measured and calculated Fluxmeter energy spectra

The monitor detector data accumulation time interval was 100 seconds. Monitor data acquisition was started before the beginning of the Fluxmeter data record so as to overlap it slightly in time on both ends. Most Fluxmeter data records have an associated monitor count rate. Linearly interpolated values of the monitor count rate were assigned to those Fluxmeter data records that have no associated monitor reading.

At each beam energy,  $E$ , the absolute normalization was obtained using the SSD-Front detector with the Fluxmeter at  $0^\circ$  to the beam. The effective BGO area at  $0^\circ$ ,  $A(E,0)$ , is given by

$$A(E,0) = \frac{N_{BGO}(0)}{N_F(0)} * A_F(E) \quad (3.6)$$

where  $N_{BGO}$  is the sum of BGO counts from all energy channels in one data record,  $N_F$  is the total number of SSD-Front counts and  $A_F(E)$  is the effective SSD-Front area as a function of beam energy.  $A_F(E)$  includes the effects of electron scattering in the Be foil, reflection at the detector surface, scattering out of the active region of the detector, effects of energy thresholds in the electronics and other detection inefficiencies. Values of  $A_F(E)$  measured at GSFC are shown in Fig. 3.5, while the solid line represents an estimate of  $A_F(E)$  used in the analysis of the RADC data. The reason that  $A_F(E)$  was chosen to approach the limiting area defined by collimator geometry is that the effects that tend to decrease the effective SSD-Front area become smaller with increasing electron energy.

The relative angle-to-angle normalization, at a fixed beam energy, was calculated using the monitor counts. For each energy a constant  $K_{FM}$  was defined such that

$$K_{FM} = \text{SSD-F counts at } 0^\circ / \text{Monitor counts at } 0^\circ \quad (3.7)$$

The BGO area as a function of energy was then given by

$$A(E,\theta) = \frac{N_{BGO}(\theta)}{K_{FM} N_{Mon}(\theta)} * A_F(E) \quad (3.8)$$

The total Fluxmeter geometric factor can be calculated by using values obtained from eq. (3.8) in eq. (2.2).

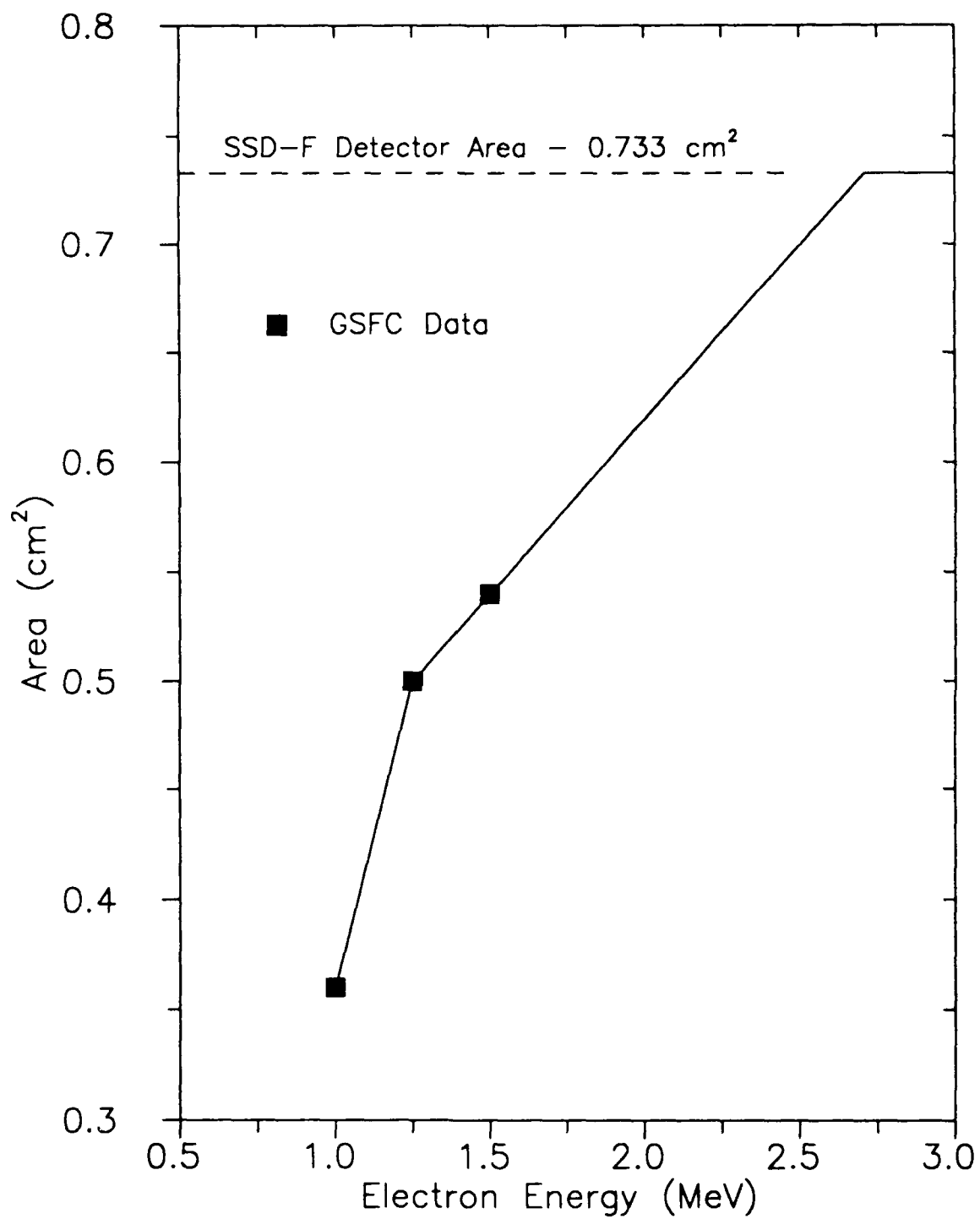


Figure 3.5 Effective SSD-F Area. Solid line is the area used in analysis of RADC data.

### 3.5 Experimental Results and Calculations

#### 3.5.1 Total Geometric Factor

The calculation of the Fluxmeter geometric factor is complicated by the fact that, as was discussed in Section 3.2, the  $A(E, \theta)$  values measured at the RADC LINAC are distorted by external scattering. As a result, the geometric factor at each electron energy was calculated in three different ways: 1) using the measured RADC angular distribution, 2) using the closest energy GSFC angular distribution (1.25 MeV for the 1.3 MeV RADC data and 1.75 MeV for the higher energy RADC data) and 3) using the calculated "no scattering" angular distribution. The geometric factors,  $GF(E)$ , obtained using method 2 or 3 were calculated from.

$$GF(E) = \frac{A(E, \theta=0)}{A_i} \cdot GF_i \quad (3.9)$$

where the index  $i$  indicates that the  $0^\circ$  area and geometric factor values are taken from the appropriate GSFC or the calculated "no scattering" angular distribution.

The measured RADC angular distributions at the effective beam energies of 1.3, 1.8, 2.8 and 3.3 MeV are very similar to the 4.2 MeV distribution (see Fig. 3.1). The 6.8 and 8.8 MeV distributions are similar to the 10.8 MeV distribution. Consequently, the geometric factor calculated using method 1 will be greatly overestimated for effective beam energies of 4.2 MeV and below. For the three highest energies, this method should be quite accurate. Method 2 will produce approximately correct geometric factors for the 1.3 and 1.8 MeV runs and probably for the 2.8, 3.3 and 4.2 MeV runs as well. The geometric factors for the three highest energies will be overestimated by this method. Finally, method 3 will underestimate the geometric factors for all energies. Use of the three methods of calculation gives a best estimate of the geometric factor at a given energy as well as upper and lower bounds. The calculated values are listed in Table 3.2.

#### 3.5.2 Energy Channel Response Calculation

The ten Fluxmeter energy channels, LL-L1 through L9-L10, can in principle be calibrated by measuring the response of the channels to mono-energetic electron beams of various energies. Unfortunately, the combination of energy straggling in the beam path and poor beam quality made such a measurement at the RADC LINAC impossible. The response of the energy channels to electrons was, therefore, calculated using available experimental data and the known physical properties of the Fluxmeter's detectors. The remainder of this section contains a description of the calculation. The results are shown and discussed in Section 4.

Table 3.2

Geometric factors calculated using methods of Section 3.5.1.

Effective Beam Energy (MeV)	Geometric Factors ( $10^{-5}$ cm <sup>2</sup> -sr)		
	Method 1	Method 2	Method 3
1.3	80.2	22.1	10.5
1.8	159.9	95.3	26.9
2.8	440.1	266.2	75.2
3.3	542.1	391.6	110.6
4.2	453.4	317.1	89.6
6.8	517.4	1235.4	349.1
8.8	671.4	1102.6	311.6
10.8	644.5	904.0	255.4

As electrons traverse the Be foil and the two solid state detectors they suffer angular scattering and energy straggling. To a good approximation the two processes can be treated independently of each other (Ref. 3.1), which implies that the energy distribution of scattered electrons is independent of the angle through which the electrons are scattered. The energy distribution is also approximately independent of the angle of incidence of the electrons on the Fluxmeter entrance aperture, since the  $\cos\theta$  corrections to the degrader thickness are less than 5% for the Fluxmeter geometry. Consequently, the shape of the measured energy distribution is only a function of the incident beam energy.

A computer code, FR4, was written to simulate the interaction of a mono-energetic beam of electrons with the Fluxmeter. This Monte Carlo calculation follows the energy loss and straggling processes of the electrons, with initial energy  $E_0$ , as they traverse the solid state detectors. It also simulates the BGO energy resolution in arriving at the final value of the electron energy as measured by the Fluxmeter. The energy losses in the Be foil are negligible and are not considered in the calculation.

An electron with energy  $E_0$  and moving toward the BGO parallel to the Fluxmeter central axis is generated at the entrance aperture. The mean energy with which the electron emerges after passing through the SSD's,  $E_1$ , is calculated using eq. (3.4). The range given by eq. (3.4),  $r(E_0)$ , has the thickness of the two SSD's (1.4 mm) subtracted

$$\Delta r = r(E_0) - 1.4 \quad (3.10)$$

and then eq. (3.4) is inverted to solve for  $E_1$  in terms of  $\Delta r$ . The shape of the distribution is given by eq. (3.1) with  $\sigma_a$  and  $b$  as calculated from eqs. (3.2) and (3.3). A random number generator which selects numbers according to the distribution given by eq. (3.1) is used to choose the deviation from the mean energy loss,  $dE_1$ , so that after the two SSD's the electron energy,  $E_2$ , is

$$E_2 = E_1 + dE_1 \quad (3.11)$$

The energy resolution of the BGO crystal is described by a gaussian curve with the standard deviation given by eq. (3.5). A gaussian random number generator is used to generate the error in energy measurement,  $dE_{BGO}$ , so that the final measured energy,  $E_m$ , is

$$E_m = E_2 + dE_{BGO} = E_1 + dE_1 + dE_{BGO} \quad (3.12)$$

At this point the appropriate energy channel, as determined by the value of  $E_m$ , is incremented and the next event is generated.

#### 4. SUMMARY OF ELECTRON CALIBRATION RESULTS

The geometric factors obtained from the measurements at GSFC and RADC are listed in Table 4.1. The column labeled GF contains the best estimate of the geometric factor at a given electron energy. The GSFC and the 6.8, 8.8 and 10.8 MeV RADC values were calculated using the measured angular distributions, while the 1.3, 1.8, 2.8, 3.3 and 4.2 MeV RADC values were calculated using method 1 of Section 3.5.1. Lower and upper limits on the RADC values are listed in the columns labeled Low GF and High GF respectively. The low limit was calculated using method 3 of Section 3.5.1, the high limit using methods 1 or 2 as indicated in the table. Values from Table 4.1 are plotted in Fig. 4.1. It should be noted that the vertical bars on the RADC data points are the Low GF and High GF limits and not statistical error bars. The solid line is an empirical fit to the best estimate geometrical factor data points and its form is given by

$$GF(E) = \begin{cases} \exp(-5.829E^2+21.452E-14.985) & \text{if } 1.00 \leq E \leq 1.75 \text{ MeV} \\ \exp(-0.378E^2+2.553E+1.373) & \text{if } 1.75 < E \leq 2.8 \text{ MeV} \\ 700 \left[ 1 - \frac{1.75}{E - 0.2} \right]^{1.2} & \text{if } E > 2.8 \text{ MeV} \end{cases} \quad (4.1)$$

Calculations, as described in Section 3.5.2, were carried out for 0.05 MeV energy steps between 0.7 and 11.0 MeV and with 100,000 events at each energy. The results show that the relative response, that is the probability of an electron with an energy E to be counted in channel n, R(E,n), of channels LL-L1 to L5-L6 can be written as a gaussian function

$$R(E,n) = R_{\max}(n) \cdot \exp\{(-E-E_p(n))^2/2\sigma^2(n)\} \quad (4.2)$$

where  $R_{\max}$  is the relative response at the peak of the response function,  $E_p$ , and  $\sigma$  is the standard deviation, obtained from the full-width-at-half-maximum, FWHM, of the calculated distribution using  $FWHM = 2.35\sigma$ . The four high energy channels, L6-L7 to L9-L10, have a broad energy acceptance and have a constant relative response,  $R_{\max}$ , in the region around  $E_{\text{peak}}$ . The relative response for these channels is given by

$$R(E,n) = \begin{cases} R_{\max}(n) \times \exp(-(E-E_p(n)-\Delta E(n))^2/2\sigma^2(n)) \\ R_{\max}(n) \\ R_{\max}(n) \times \exp(-E-E_p(n)+\Delta E(n))^2/2\sigma^2(n) \end{cases} \quad (4.3)$$

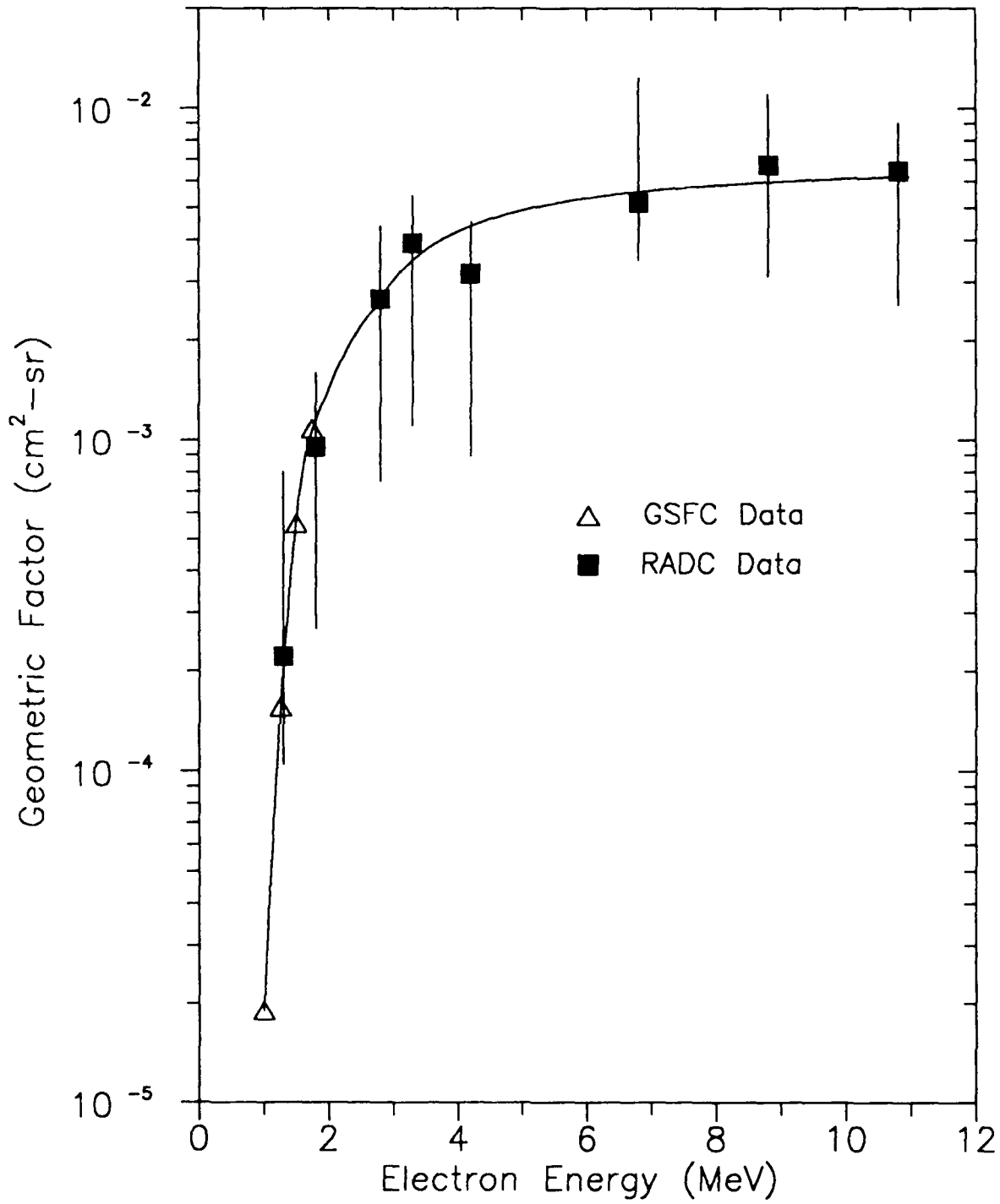


Figure 4.1 Total Fluxmeter geometric factor. Solid line is an empirical fit to the data (see text).

Table 4.1

List of geometric factors from GSFC and RADC experiments. Geometric factors are in units of  $10^{-5}$  cm<sup>2</sup>-sr. Letter in column labeled Ang. Dist. indicates which angular distribution was used in calculating the High GF value.

Effective Beam Energy (MeV)	Facility	GF	Low GF	High GF	Ang. Dist.
1.00	GSFC	1.85	----	----	--
1.25	GSFC	15.5	----	----	--
1.3	RADC	22.1	10.5	80.2	a
1.50	GSFC	55.6	----	----	--
1.75	GSFC	108.2	----	----	--
1.8	RADC	95.3	26.9	159.9	a
2.8	RADC	266.2	75.2	440.1	a
3.3	RADC	391.6	110.6	542.1	a
4.2	RADC	317.1	89.6	453.4	a
6.8	RADC	517.4	349.1	1235.6	b
8.8	RADC	671.4	311.6	1102.6	b
10.8	RADC	644.5	255.4	904.0	b

Notes: a - own angular distribution  
b - 1.75 GSFC angular distribution

for  $E < E_p(n) - \Delta E$ ,  $E_p(n) - \Delta E < E < E_p(n) + \Delta E$  and  $E > E_p(n) + \Delta E$  respectively. The various parameters used in eqs. (4.2) and (4.3) are listed in Table 4.2. A full tabulation of  $GF(E)$  and  $R(E,n)$  values is found in the Appendix. The absolute energy response of a Fluxmeter energy channel,  $AR(E,n)$ , is given by

$$AR(E,n) = GF(E) \cdot R(E,n) \quad (4.4)$$

Figs. 4.2 and 4.3 show the curves which describe the absolute response of the Fluxmeter according to eq. (4.4).

## 5. PROTON RESPONSE MEASUREMENT

The response of the Fluxmeter to protons with energies between 25 and 144 MeV was investigated in May, 1985 at the Harvard University Cyclotron. The accelerator produces a 160 MeV proton beam which must be passed through absorber material in order to lower the energy of the beam particles. Beam energies of 66 MeV and below were obtained by using a 4 inches of polyethylene as well aluminum and/or copper pieces of varying thickness as absorber material. Higher beam energies were obtained by using aluminum and/or copper absorbers only. The Fluxmeter and monitor detectors were located approximately 50 inches from the last piece of absorber material. The primary monitor detector was a 750  $\mu\text{m}$  thick solid state detector with a 0.5 inch diameter lead collimator in front of it. The collimator was 2 inches thick, which was sufficient to stop the most energetic beam protons. The beam intensity was chosen so that no more than one particle was detected by the monitor detector for each cyclotron beam spill period (4-5  $\mu\text{sec}$ ). The analysis of the singles count rates of the two Fluxmeter solid state detectors and the BGO crystal is contained in Section 5.1. A discussion of the coincidence data, which describes the contamination of the electron channels by protons, is in Section 5.2.

The response of the Fluxmeter may be conveniently divided into two energy regions: low energy, below 80 MeV; and high energy, above 80 MeV. At low energies, the protons cannot penetrate through the 0.2 inch tungsten collimators, so that the collimator geometry determines the response of the instrument. At high energies, as the protons penetrate through one or more collimators and the side and back shielding, the geometry of the various detectors determines the instrument response.

### 5.1 Singles Data

The proper response of the front and back solid state detectors to protons can be verified by considering the ratio of counts of SSD-Back to counts of SSD-Front. This ratio, for runs with the Fluxmeter at  $0^\circ$ , is shown in Fig. 5.1 as a function of beam energy. At low energies, the effective areas of the Fig. 4.2

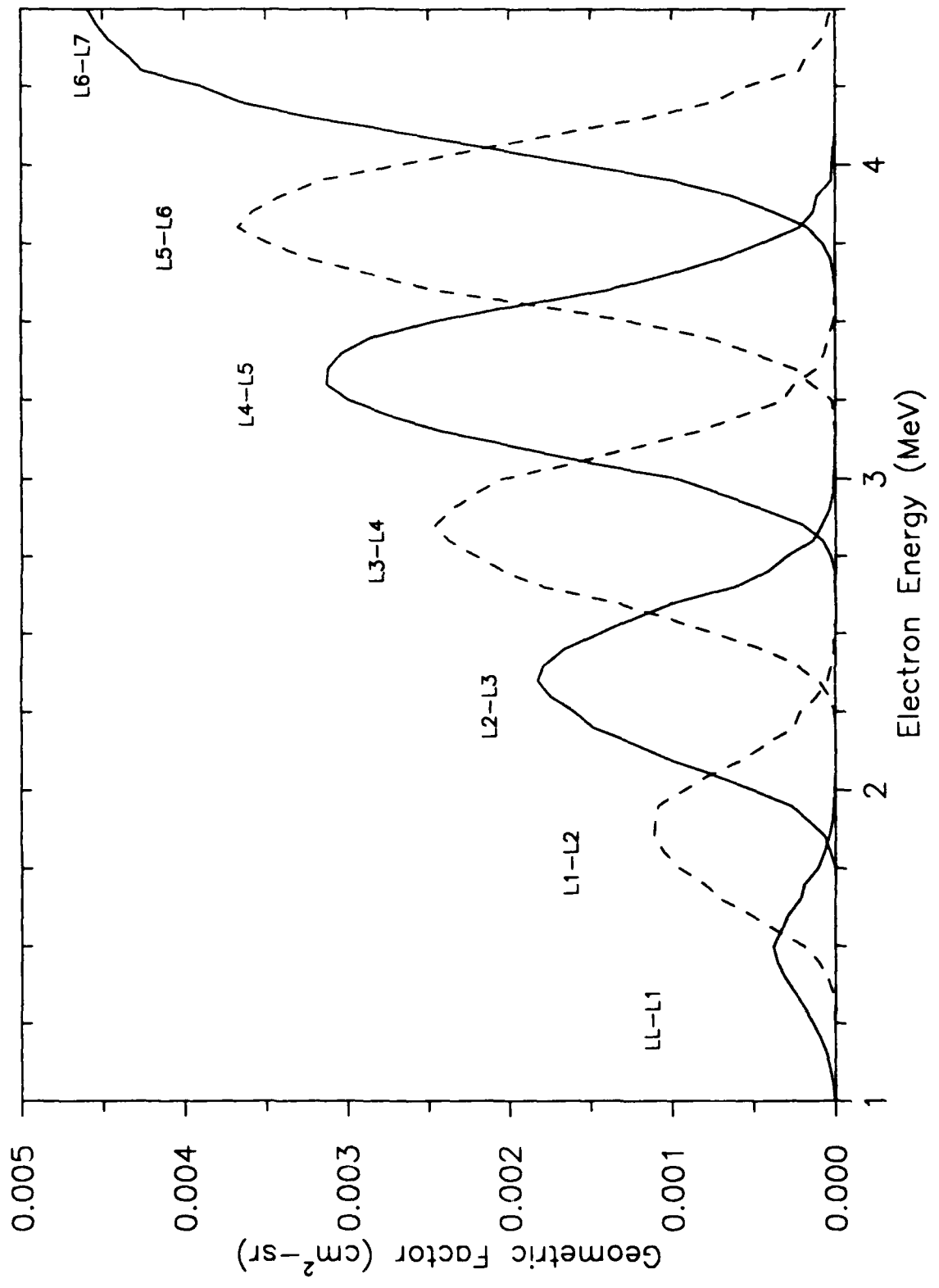


Figure 4.2 Absolute response of Fluxmeter channels LL-L1 thru L6-L7

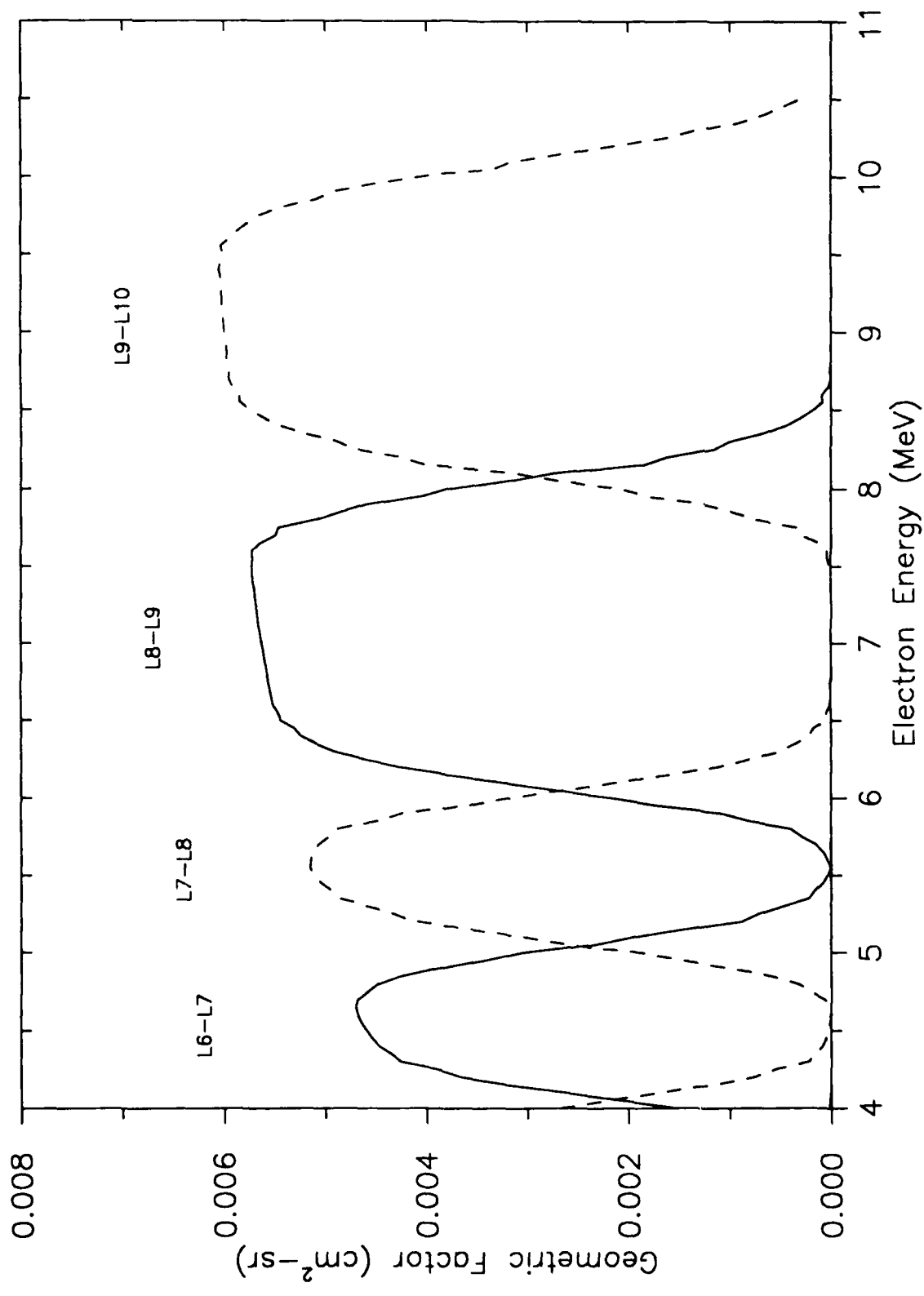


Figure 4.3 Absolute response of Fluxmeter channels L6-L7 thru L9-L10

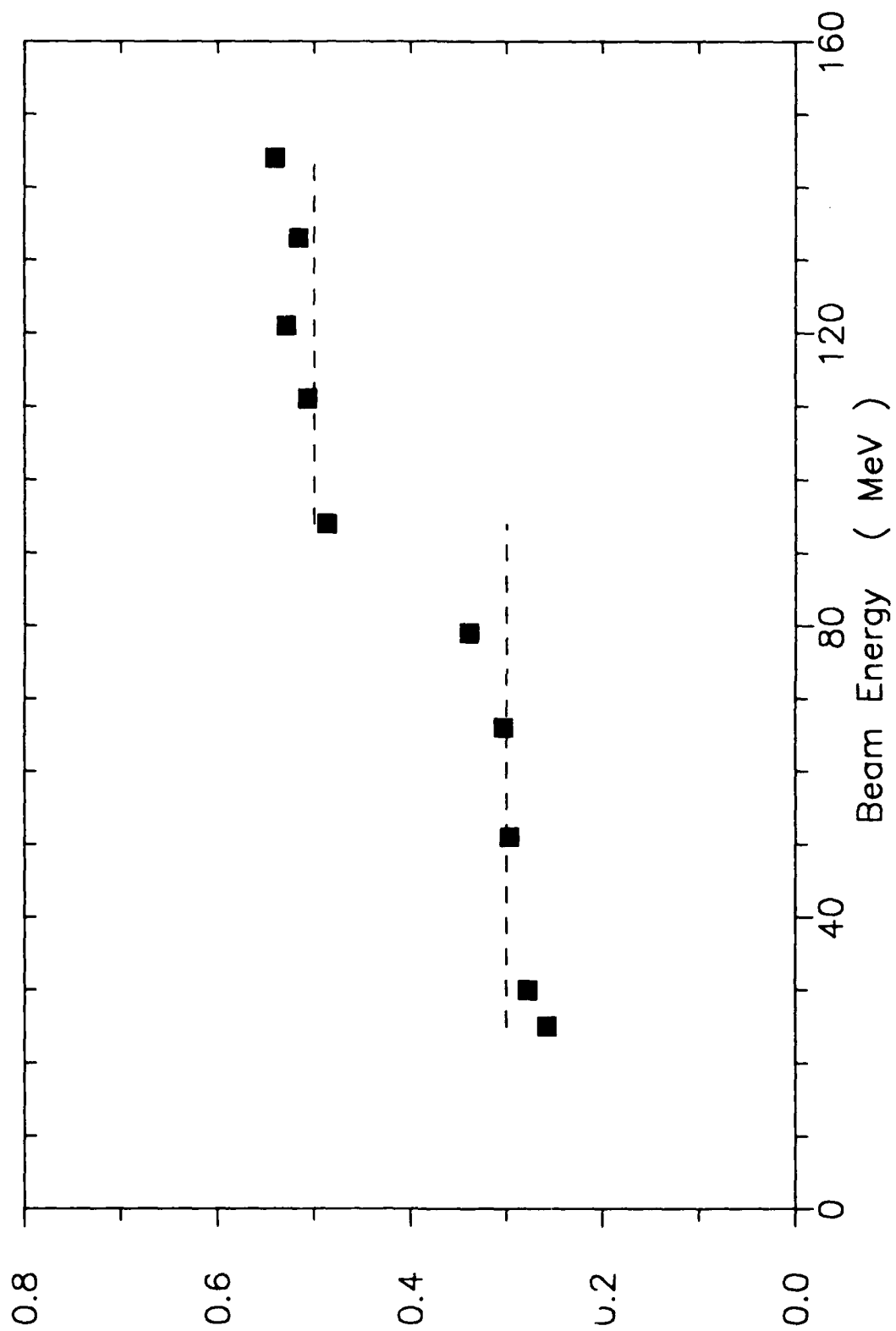


Figure 5.1 Ratio of counts of SSD-Front to SSD-Back detectors.  
The dashed line shows the theoretically expected value of the ratio.

Table 4.2

List of parameters used in eqs. (4.2) and (4.3) to describe the response of the Fluxmeter energy channels.

Channel	$E_p$ (MeV)	$R_{max}$	$\sigma$ (MeV)	$\Delta E$ (MeV)
LL-L1	1.30	0.919	0.234	---
L1-L2	1.82	0.914	0.234	---
L2-L3	2.35	0.925	0.234	---
L3-L4	2.80	0.896	0.221	---
L4-L5	3.30	0.886	0.234	---
L5-L6	3.80	0.905	0.221	---
L6-L7	4.55	0.997	0.293	0.15
L7-L8	5.55	0.997	0.340	0.15
L8-L9	7.08	1.000	0.357	0.58
L9-L10	9.05	1.000	0.425	0.50

detectors are determined by the collimators. From values listed in Table 2.3, it is evident that the ratio of collimator hole areas is 0.3. At high energies the ratio of effective areas is just the ratio of detector areas or 0.5. The theoretically expected ratio of count rates is also plotted in Fig. 5.1. The agreement between data and calculation is satisfactory, indicating that the effective areas of the two solid state detectors are 0.733 cm<sup>2</sup> (SSD-Front) and 0.219 cm<sup>2</sup> (SSD-Back) at low energies and 1.0 and 0.5 cm<sup>2</sup> at high energies.

The effective BGO area,  $A_{bgo}$ , for protons of a given energy can be obtained from the data by using

$$A_{bgo} = (N_{bgo}/N_f) * A_f \quad (5.1)$$

where  $N_{bgo}$  is the total number of BGO counts,  $N_f$  is the number of SSD-Front counts and  $A_f$  is the effective SSD-Front area. The effective BGO areas at 0° with respect to the beam, as obtained from the data as well as the theoretically expected values, are shown in Fig. 5.2 and listed in Table 5.1. Theoretical values were obtained in the following way. In the energy region 25 to 80 MeV the protons cannot penetrate through the collimators and the effective BGO area is defined by the SSD-Back collimator. In the region between 80 and 115 MeV, protons can go through only one collimator and the effective area is defined by the SSD-Front collimator. Finally, in the region from 115 to 144 MeV, protons can travel through two collimators and the effective area is defined by the entrance collimator.

Two features are immediately apparent from Fig. 5.2 One is the deviation from the expected value of the effective area above 80 MeV and the other is the deviation at the two lowest energies. The high energy deviation is caused by a number of factors. The BGO photomultiplier tube pulses for high energy protons are large enough to saturate the amplifiers. This can cause the Fluxmeter to miss proton counts that come in the same beam spill as a large pulse event. Although the beam intensity was set to minimize such occurrences, a 20-30% rate of such beam spills cannot be ruled out. Another reason for the deviation is that a proton penetrating through a tungsten collimator must also go through a number of aluminum spacers before it gets to the BGO crystal. This effectively raises the energy threshold for penetration through a collimator. Finally, multiple scattering effects can also serve to decrease the effective BGO area.

The low energy deviation is most likely caused by beam associated background radiation, probably gamma rays. This can be seen from the following argument. The collimator geometry does not allow any SSD-Front - BGO crystal coincidences for angles of incidence above 10.5 degrees. However, examination of Fig. 5.3 clearly shows that  $A_{bgo} = 0.2$  cm<sup>2</sup> for forbidden angles. Fig. 5.4 shows the fraction of the total BGO counts in the lowest two and the highest BGO channels. Since protons with 25 and 30 MeV deposit enough energy to exceed the L10 level the excess LL-L1

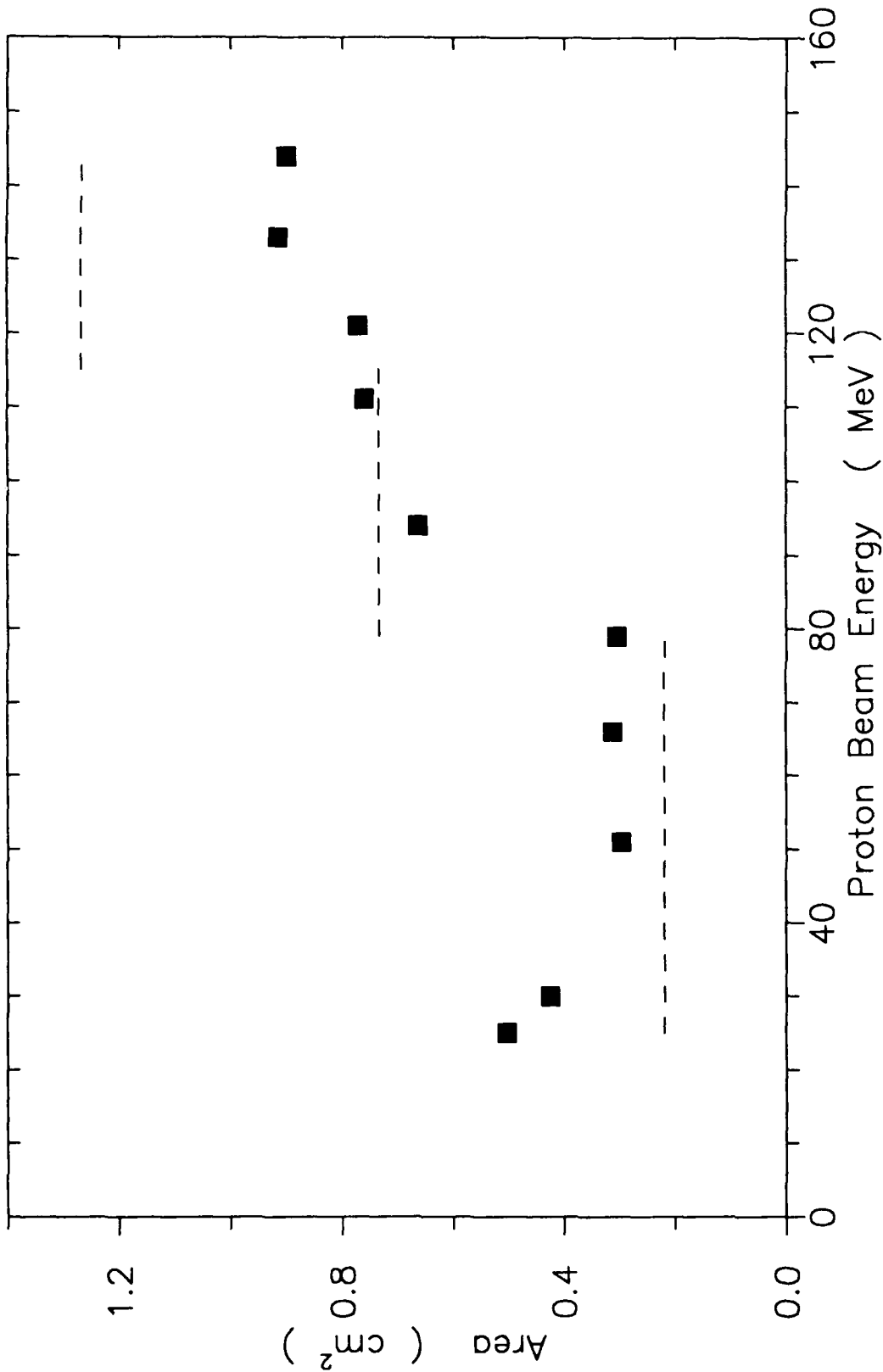


Figure 5.2 Effective BGO crystal area with the Fluxmeter at 0° with respect to the beam. The dashed lines show the theoretically calculated area.

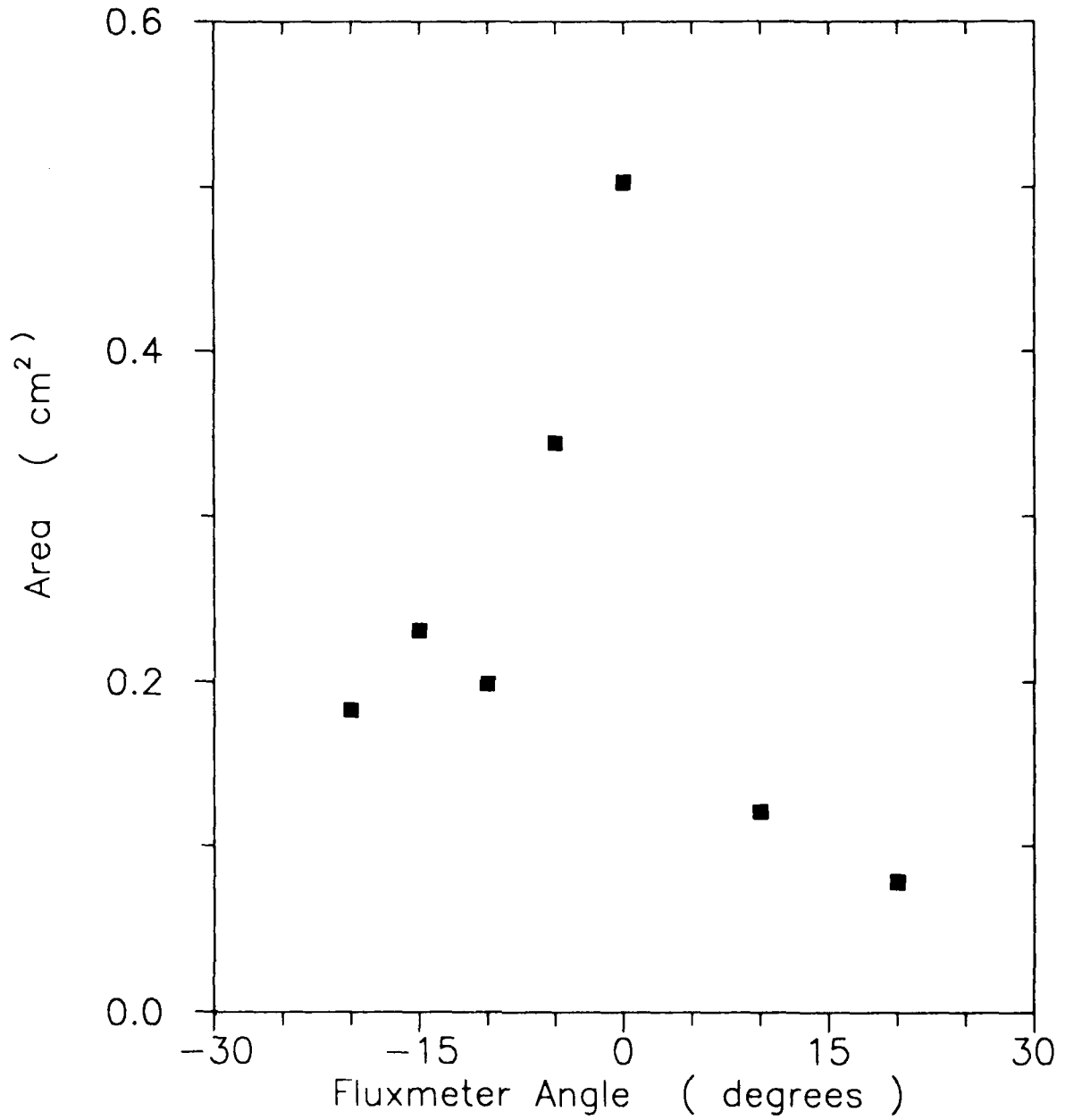


Figure 5.3 Measured BGO crystal area as a function of Fluxmeter angle. Proton beam energy is 25 MeV.

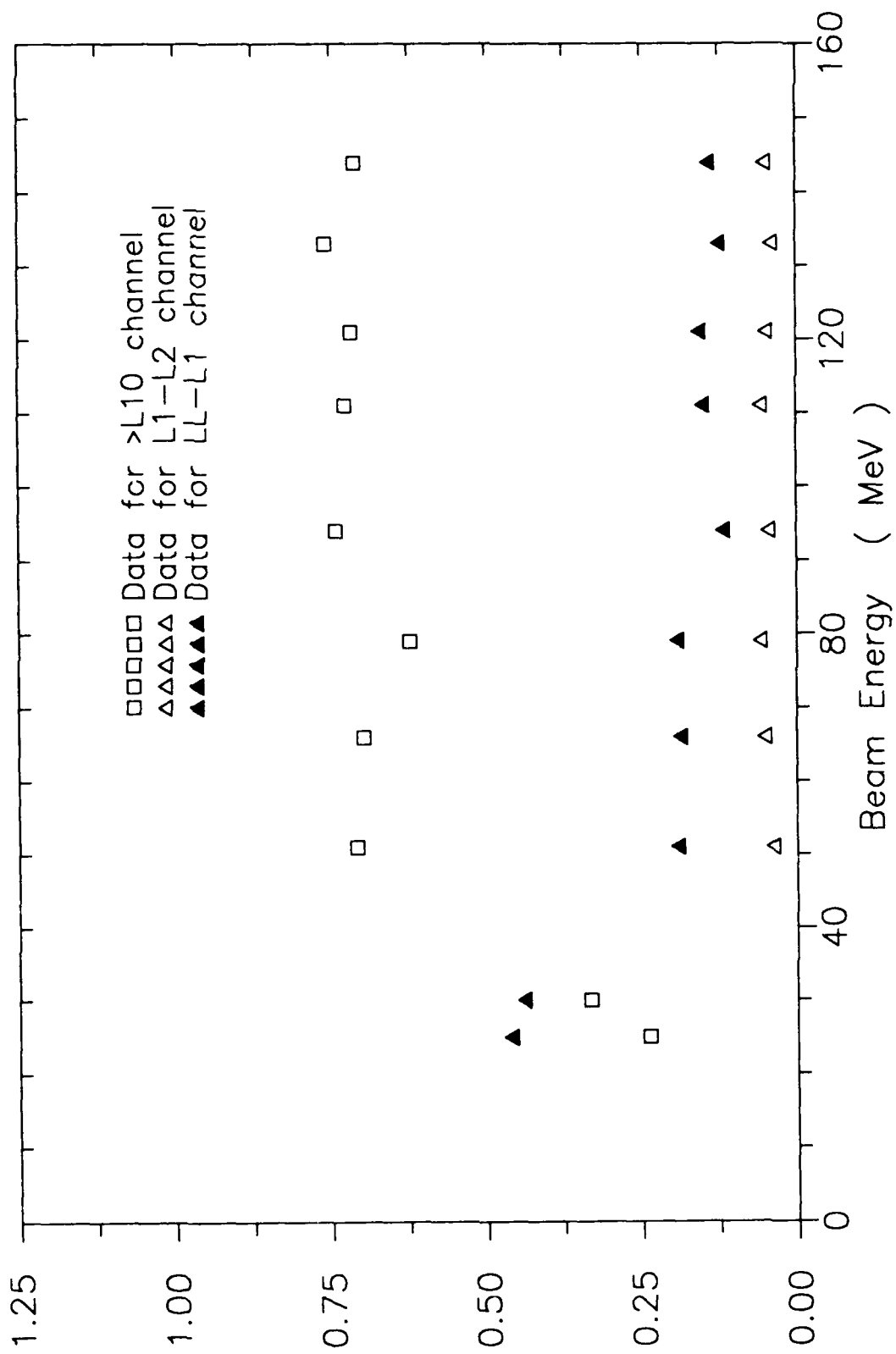


Figure 5.4 Fraction of the total BGO counts found in the two lowest and the highest BGO pulse height channels. The Fluxmeter was in singles mode and at 0° with respect to the proton beam.

TABLE 5.1

Measured and calculated areas of the Fluxmeter,  
with the instrument at  $0^\circ$  with respect to the beam.

Energy (MeV)	Measured Area (cm <sup>2</sup> )	Calculated Area (cm <sup>2</sup> )
25	0.503	0.219
30	0.425	0.219
51	0.296	0.219
66	0.311	0.219
79	0.305	0.219
94	0.662	0.733
111	0.759	0.733
121	0.771	1.267
133	0.913	1.267
144	0.900	1.267

counts and the relatively normal L1-L2 counts at 25 and 30 MeV indicate that the background is due to radiation that deposits less than 1 MeV in the BGO per particle. This radiation is most likely gamma rays from inelastic collisions between beam protons and the carbon and aluminum nuclei in the beam degrader plates. This background is large at low beam energies primarily because the intensity of the beam striking the degrader plates had to be greatly increased to maintain a suitable Fluxmeter counting rate at the two lowest energies, 25 and 30 MeV. If the  $0.2 \text{ cm}^2$ , due to the background is subtracted from  $A_{\text{BGO}}$  values at 25 and 30 MeV, the resulting values are in good agreement with theoretical expectations.

At low energies, the BGO geometric factor, for protons in singles mode, is determined by the entrance and SSD-Back collimators. The angular dependence of the effective area as can be calculated using eq. (2.3) with  $r_1 = 0.635 \text{ cm}$ ,  $r_2 = 0.264 \text{ cm}$  and  $D = 4.83 \text{ cm}$ . Evaluating this equation shows that the effective area is roughly constant from  $0^\circ$  to  $5^\circ$  and decreases nearly linearly to 0 between  $5^\circ$  and  $10.5^\circ$ . Using the measured effective area at  $0^\circ$ ,  $0.3 \text{ cm}^2$ , and the calculated angular behavior as inputs to eq. (2.2) yields a Fluxmeter geometric factor of  $1.8 \times 10^{-2} \text{ cm}^2\text{-sr}$  for protons with kinetic energies between 25 and 80 MeV. At higher proton energies, the angular dependence of the effective area of the BGO is a complicated function of angle and energy. A full measurement of the response of the instrument was not undertaken. However, the high energy,  $0^\circ$  results indicate (see Fig. 2.2) that the geometric factor calculated using simple geometrical assumptions is a reliable upper limit on the singles response of the Fluxmeter to high energy protons.

A final result extracted from the singles data is the pulse height spectrum in the BGO crystal for incident protons. As is evident from Fig. 5.4, the pulse height distribution varies little with proton energy (except for the 25 and 30 MeV data points as discussed above). Table 5.2 shows the measured distribution of counts in the various BGO channels averaged for runs with beam energies between 51 and 144 MeV.

## 5.2 Coincidence Data

In addition to the data taken with the Fluxmeter in a singles mode, data were also taken with various coincidence requirements. The possible coincidence modes were SSD-Front and BGO (CRF), SSD-Back and BGO (CRB), SSD-Front, SSD-Back and BGO (CRFB) and SSD-Front, SSD-Back, anti-coincidence shield and BGO (CRA). Tables 5.3, 5.4, 5.5 and 5.6 show the proton geometric factors as a function of proton energy for each BGO channel and for each coincidence requirement. It is evident that the use of a coincidence mode greatly reduces the sensitivity of the instrument to incident protons.

The values in the Tables 5.3-5.6 were calculated in the following way. The geometric factor of a BGO channel,  $L$ , at a given proton energy,  $E$ , and for a given coincidence mode,  $C$ ,  $GLC(E)$  is given by

TABLE 5.2

Measured distribution of counts in the BGO channels averaged for runs with beam energies between 51 and 144 MeV. Data taken with the Fluxmeter in singles mode.

<u>Channel</u>	<u>Fraction in Channel</u>
>L10	0.710
L9-L10	0.008
L8-L9	0.011
L7-78	0.006
L6-L7	0.009
L5-L6	0.008
L4-L5	0.009
L3-L4	0.001
L2-L3	0.022
L1-L2	0.049
LL-L1	0.158

TABLE 5.3

Fluxmeter proton geometric factors for CRF ON.  
The units are  $10^{-6} \text{ cm}^2\text{-sr}$ .

Channel	Proton Energy (MeV)									
	25	30	51	66	79	94	111	121	133	144
>L10	8.8	<28.0	4.5	<4.5	<5.6	<27.0	<50.0	120.0	4200.0	4000.0
I9-L10	<4.5	<28.0	<4.5	<4.5	<5.6	<27.0	<50.0	<24.0	75.0	32.0
I8-I9	<4.5	<28.0	<4.5	<4.5	<5.6	<27.0	<50.0	<24.0	75.0	64.0
I7-I8	<4.5	<28.0	<4.5	<4.5	<5.6	<27.0	<50.0	<24.0	<15.0	<6.4
I6-I7	<4.5	<28.0	<4.5	<4.5	<5.6	<27.0	<50.0	<24.0	37.0	<6.4
I5-I6	<4.5	<28.0	<4.5	<4.5	<5.6	<27.0	<50.0	<24.0	<15.0	16.0
I4-I5	<4.5	<28.0	<4.5	<4.5	<5.6	<27.0	<50.0	<24.0	<15.0	16.0
I3-I4	<4.5	<28.0	<4.5	<4.5	<5.6	<27.0	<50.0	<24.0	37.0	16.0
I2-I3	<4.5	<28.0	<4.5	<4.5	<5.6	<27.0	<50.0	59.0	75.0	64.0
I1-I2	<4.5	<28.0	<4.5	<4.5	<5.6	<27.0	<50.0	180.0	220.0	81.0
LL-L1	<4.5	<28.0	<4.5	11.0	14.0	130.0	<50.0	470.0	490.0	640.0
LL-L10	<4.5	<28.0	<4.5	11.0	14.0	130.0	<50.0	709.0	1009.0	929.0
TOTAL	8.8	<28.0	<4.5	11.0	14.0	130.0	<50.0	829.0	5209.0	4929.0

Notes: (1) LL-L10 is the sum of channels LL-L1 to L9-L10.

(2) Upper limit values correspond to zero counts; see Eq. (5.4).

Table 5.4  
 Fluxmeter proton geometric factors for CRB ON.  
 The units are  $10^{-6} \text{ cm}^2\text{-sr}$ .

Channel	Proton Energy (MeV)													
	25	30	51	66	79	94	111	121	133	144				
>I10	<8.9	<28.0	<3.5	11.0	<4.1	<25.0	320.0	920.0	240.0	300.0				
I9-I10	<8.9	<28.0	<3.5	<4.4	<4.1	<25.0	<12.0	<13.0	<7.0	5.3				
I8-I9	<8.9	<28.0	<3.5	<4.4	<4.1	<25.0	<12.0	<13.0	<7.0	5.3				
I7-I8	<8.9	<28.0	<3.5	<4.4	<4.1	<25.0	<12.0	<13.0	<7.0	<2.1				
I6-I7	<8.9	<28.0	<3.5	<4.4	<4.1	<25.0	<12.0	<13.0	<7.0	<2.1				
I5-I6	<8.9	<28.0	<3.5	<4.4	<4.1	<25.0	<12.0	<13.0	<7.0	<2.1				
I4-I5	<8.9	<28.0	<3.5	11.0	<4.1	<25.0	<12.0	<13.0	<7.0	<2.1				
I3-I4	<8.9	<28.0	<3.5	11.0	10.0	<25.0	<12.0	<13.0	<7.0	<2.1				
I2-I3	<8.9	<28.0	<3.5	11.0	<4.1	<25.0	<12.0	<13.0	<7.0	5.3				
I1-I2	<8.9	<28.0	<3.5	<4.4	10.0	<25.0	<12.0	<13.0	35.0	<2.1				
LL-I1	<8.9	<28.0	17.0	22.0	<4.1	72.0	61.0	63.0	52.0					
120.0														
LL-I10	<8.9	<28.0	17.0	55.0	20.0	72.0	61.0	63.0	87.0	435.9				
TOTAL	<8.9	<28.0	17.0	66.0	20.0	72.0	381.0	983.0	327.0	435.9				

Notes: (1) LL-I10 is the sum of channels LL-I1 to I9-I10.

(2) Upper limit values correspond to zero counts; see Eq. (5.4).

TABLE 5.5

Fluxmeter proton geometric factors for CRF and CRB ON.  
The units are  $10^{-6} \text{ cm}^2\text{-sr}$ .

Channel	Proton Energy ( MeV )									
	25	30	51	66	79	94	111	121	133	144
>L10	<9.0	<35.0	<2.0	<4.8	<5.7	<28.0	<5.8	<14.0	<30.0	9.7
I9-I10	<9.0	<35.0	<2.0	<4.8	<5.7	<28.0	<5.8	<14.0	<30.0	<1.9
I8-I9	<9.0	<35.0	<2.0	<4.8	<5.7	<28.0	<5.8	<14.0	<30.0	<1.9
I7-I8	<9.0	<35.0	<2.0	<4.8	<5.7	<28.0	<5.8	<14.0	<30.0	<1.9
I6-I7	<9.0	<35.0	<2.0	<4.8	<5.7	<28.0	<5.8	<14.0	<30.0	<1.9
I5-I6	<9.0	<35.0	<2.0	<4.8	<5.7	<28.0	<5.8	<14.0	<30.0	<1.9
I4-I5	<9.0	<35.0	<2.0	<4.8	<5.7	<28.0	<5.8	<14.0	<30.0	<1.9
I3-I4	<9.0	<35.0	<2.0	<4.8	<5.7	<28.0	<5.8	<14.0	<30.0	<1.9
I2-I3	<9.0	<35.0	<2.0	<4.8	<5.7	<28.0	14.0	<14.0	<30.0	4.8
I1-I2	<9.0	<35.0	<2.0	<4.8	<5.7	<28.0	<5.8	<14.0	<30.0	19.0
II-I1	<9.0	<35.0	4.9	<4.8	<5.7	<28.0	14.0	<14.0	<30.0	39.0
II-I10	<9.0	<35.0	4.9	<4.8	<5.7	<28.0	28.0	<14.0	<30.0	62.8
TOTAL	<9.0	<35.0	4.9	<4.8	<5.7	<28.0	28.0	<14.0	<30.0	72.5

Notes: (1) II-I10 is the sum of channels II-I1 to I9-I10.

(2) Upper limit values correspond to zero counts; see Eq. (5.4).

TABLE 5.6

Fluxmeter proton geometric factors for all coincidences ON.  
The units are  $10^{-6} \text{ cm}^2\text{-sr}$ .

Channel	Proton Energy ( MeV )									
	25	30	51	66	79	94	111	121	133	144
>L10	<7.1	<22.0	<2.0	<5.4	<1.5	<27.0	<10.0	<9.1	<10.0	14.0
L9-L10	<7.1	<22.0	<2.0	<5.4	<1.5	<27.0	<10.0	<9.1	<10.0	<5.8
L8-L9	<7.1	<22.0	<2.0	<5.4	<1.5	<27.0	<10.0	<9.1	<10.0	<5.8
L7-L8	<7.1	<22.0	<2.0	<5.4	<1.5	<27.0	<10.0	<9.1	<10.0	<5.8
L6-L7	<7.1	<22.0	<2.0	<5.4	<1.5	<27.0	<10.0	<9.1	<10.0	<5.8
L5-L6	<7.1	<22.0	<2.0	<5.4	<1.5	<27.0	<10.0	<9.1	<10.0	<5.8
L4-L5	<7.1	<22.0	<2.0	<5.4	<1.5	<27.0	<10.0	<9.1	<10.0	<5.8
L3-L4	<7.1	<22.0	<2.0	13.0	<1.5	<27.0	<10.0	<9.1	<10.0	<5.8
L2-L3	<7.1	<22.0	<2.0	<5.4	<1.5	<27.0	<10.0	<9.1	<10.0	<5.8
L1-L2	<7.1	<22.0	<2.0	<5.4	<1.5	<27.0	<10.0	<9.1	<10.0	<5.8
LL-L1	<7.1	<22.0	5.0	<5.4	3.7	<27.0	<10.0	23.0	26.0	14.0
LL-L10	<7.1	<22.0	5.0	13.0	3.7	<27.0	<10.0	23.0	26.0	14.0
TOTAL	<7.1	<22.0	5.0	13.0	3.7	<27.0	<10.0	23.0	26.0	28.0

Notes: (1) LL-L10 is the sum of channels LL-L1 to L9-L10.

(2) Upper limit values correspond to zero counts; see Eq. (5.4).

$$G_{LC}(E) = P_L \cdot S_{LC}(E) \cdot A_0(E) \cdot F_C(E) \quad (5.2)$$

$P_L$  is the probability that the BGO signal will be in a given channel L (values listed in Table 5.2)  $A_0(E)$  is the measured Fluxmeter singles area at  $0^\circ$  (Table 5.1),  $S_{LC}(E)$  is the suppression factor, at  $0^\circ$ , of a coincidence mode (CRF, CRB, CRFB or CRA) relative to the singles mode and  $F_C(E)$  is the term that converts the area at  $0^\circ$  to the geometric factor.

The suppression factor is given by

$$S_{LC}(E) = (N_{LC}(E) / N_{LS}(E)) * (M_S(E) / M_C(E)) \quad (5.3)$$

where  $N_{LC}$  is the number of BGO counts in channel L in coincidence mode C,  $N_{LS}$  is the number of BGO counts in channel L in singles mode and  $M_C$  and  $M_S$  are the SSD-Front counts in the coincidence and singles modes respectively. If  $N_{LC}(E) = 0$ , Eq. 5.3 has to be modified. A conservative upper limit on  $S_{LC}$  can be obtained assuming that the actual count distribution is a Poisson distribution and that the probability of getting zero counts is 0.67. In that case Eq. (5.3) is replaced by

$$S_{LC}(E) = (-\ln(0.67)/N_{LS}(E)) * (M_S(E)/M_C(E)) \quad (5.4)$$

and the geometric factor is taken as an upper limit. In calculating the geometric factor sums, the upper limit values were not included except to provide an upper limit for the sum.

The term  $F_C(E)$  is simply the ratio of the geometric factor calculated using Eq. (2.4) and the effective Fluxmeter area at  $0^\circ$ , in a given coincidence mode, as seen by the incident beam. The radii  $r_1$  and  $r_2$  used in Eq. (2.4) are the defining apertures for a particular coincidence mode. The dependence on beam energy comes from the fact that, for proton energies below 80 MeV, the defining apertures are the collimators while above 80 MeV, since the collimators no longer stop the beam, the defining apertures are the detectors themselves. Table 5.7 lists the relevant geometric information for the calculation of the  $F_C(E)$  values as well as the values themselves.

## 6. CONCLUSION

The analysis of the experimented work carried out at the GSFC. Van De Graaff, the RADC LINAC and the Harvard Cyclotron provide a calibration of the Fluxmeter for electrons with energies between 1 and 10 MeV and indicate the instruments' relative insensitivity to protons with energies below 144 MeV. A further refinement of the calibration may be carried out on orbit, by comparing the Fluxmeter data with data from other instruments which overlap the Fluxmeter's energy range.

TABLE 5.7

Listing of  $F_C$  values, and the geometric information used to derive them, for the various beam energies and coincidence modes.

Beam Energy and Coinc. Mode	First Defining Aperture		Second Defining Aperture		Distance (cm)	Calculated Area (cm <sup>2</sup> )	$F_C$ (sr)
	Number	Radius (cm)	Number	Radius (cm)			
Low Energy:	1	0.635	8	0.264	4.83	0.219	0.053
All Modes							
High Energy:	1	0.635	11	1.270	5.67	1.267	0.153
ALL OFF and CRF modes							
High Energy: All other modes	5	0.564	9	0.399	5.207	0.500	0.046

Notes: (1) Number of aperture refers to Table 2.3

(2) Distance is the length of gap between the two defining apertures.

## REFERENCES

- 1.1 J. L. Hunerwadel, B. Sellers, and F. A. Hanser, "Design, Fabricate, Calibrate, Test and Deliver Two Satellite Electron Flux Detectors", Report AFGL-TR-87-0205, (June 1987). Final Report for Contract F19628-79-C-0175. ADA190799.
- 1.2 P. R. Morel, F. A. Hanser, B. Sellers, J. Hunerwadel, R. Cohen, B. D. Kane and B. K. Dichter, "Fabricate, Calibrate and Test a Dosimeter for Integration into the CRRES Satellite", Report GL-TR-89-0152. Final Report for Contract F19628-82-C-0090. ADA213812
- 2.1 S. M. Seltzer and M. J. Berger, "Transmission and Reflection of Electrons by Foils", NIM 119, 157 (1974).
- 2.2 M. J. Berger and S. M. Seltzer, in Studies in Penetration of Charged Particles in Matter, National Academy of Sciences - National Research Council Publication 1133 (1964), p. 205.
- 2.3 D. H. Rester and J. H. Derrickson, "Electron Transmission Measurements for Al, Sn and Au Targets at Electron Bombarding Energies of 1.0 and 2.5 MeV", J. Appl. Phys. 42, 714 (1971).
- 3.1 M. J. Berger, S. M. Seltzer, S. E. Chappell, J. C. Humphreys and J. W. Motz, "Response of Silicon Detectors to Monoenergetic Electrons with Energies between 0.15 and 5.0 MeV", NIM 69, 181 (1969).
- 3.2 F. Buskirk, M. Cavalli-Sforza, D. Coyne, I. Kirkbride and C. Newman, "Energy Resolution Measurements on a Large Single BGO Crystal From 1 MeV to 50 MeV", IEEE Trans. Nucl. Sci. NS-29, 346 (1982).
- 3.3 A. E. Evans, IEEE Nuclear Science Symposium, Paper No. 2C-2, 1979.

## APPENDIX

The appendix contains a tabulation of the Fluxmeter geometric factors and relative channel responses as a function of incident electron energy. The column labelled GF has the total geometric factor, in units of  $\text{cm}^2 - \text{sr}$ , calculated using the eq. 4.1. The relative channel responses, calculated using eqs. (4.2) and (4.3), are in columns labelled L1 through L10 (L1 indicates channel LL-L1, L2 channel L1-L2 etc.). The absolute energy response of an energy channel can be calculated from the table in the appendix, according to eq. (4.4), by multiplying the GF value at, a given energy, by the relative channel response at the same energy.

Energy (MeV)	GF	L1	L2	L3	L4	L5	L6	L7	L8	L9	L10
0.70	0.00000059	0.033	0.000	0.000	0.000	0.000	0.000	0.000	0.000	0.000	0.000
0.75	0.00000113	0.054	0.000	0.000	0.000	0.000	0.000	0.000	0.000	0.000	0.000
0.80	0.00000210	0.082	0.000	0.000	0.000	0.000	0.000	0.000	0.000	0.000	0.000
0.85	0.00000379	0.155	0.000	0.000	0.000	0.000	0.000	0.000	0.000	0.000	0.000
0.90	0.00000665	0.225	0.000	0.000	0.000	0.000	0.000	0.000	0.000	0.000	0.000
0.95	0.00001133	0.342	0.000	0.000	0.000	0.000	0.000	0.000	0.000	0.000	0.000
1.00	0.00001874	0.450	0.000	0.000	0.000	0.000	0.000	0.000	0.000	0.000	0.000
1.05	0.00003010	0.581	0.000	0.000	0.000	0.000	0.000	0.000	0.000	0.000	0.000
1.10	0.00004697	0.687	0.000	0.000	0.000	0.000	0.000	0.000	0.000	0.000	0.000
1.15	0.00007119	0.760	0.003	0.000	0.000	0.000	0.000	0.000	0.000	0.000	0.000
1.20	0.00010478	0.862	0.001	0.000	0.000	0.000	0.000	0.000	0.000	0.000	0.000
1.25	0.00014978	0.910	0.012	0.000	0.000	0.000	0.000	0.000	0.000	0.000	0.000
1.30	0.00020795	0.919	0.028	0.000	0.000	0.000	0.000	0.000	0.000	0.000	0.000
1.35	0.00028040	0.899	0.069	0.000	0.000	0.000	0.000	0.000	0.000	0.000	0.000
1.40	0.00036721	0.850	0.136	0.000	0.000	0.000	0.000	0.000	0.000	0.000	0.000
1.45	0.00046707	0.771	0.226	0.000	0.000	0.000	0.000	0.000	0.000	0.000	0.000
1.50	0.00057700	0.661	0.335	0.000	0.000	0.000	0.000	0.000	0.000	0.000	0.000
1.55	0.00069228	0.476	0.523	0.000	0.000	0.000	0.000	0.000	0.000	0.000	0.000
1.60	0.00080669	0.362	0.638	0.000	0.000	0.000	0.000	0.000	0.000	0.000	0.000
1.65	0.00091297	0.234	0.766	0.000	0.000	0.000	0.000	0.000	0.000	0.000	0.000
1.70	0.00100353	0.191	0.808	0.001	0.000	0.000	0.000	0.000	0.000	0.000	0.000
1.75	0.00107132	0.101	0.894	0.005	0.000	0.000	0.000	0.000	0.000	0.000	0.000
1.80	0.00114856	0.060	0.914	0.026	0.000	0.000	0.000	0.000	0.000	0.000	0.000
1.85	0.00121796	0.034	0.913	0.053	0.000	0.000	0.000	0.000	0.000	0.000	0.000
1.90	0.00128911	0.015	0.858	0.127	0.000	0.000	0.000	0.000	0.000	0.000	0.000
1.95	0.00136184	0.006	0.795	0.199	0.000	0.000	0.000	0.000	0.000	0.000	0.000
2.00	0.00143595	0.004	0.645	0.351	0.000	0.000	0.000	0.000	0.000	0.000	0.000
2.05	0.00151125	0.000	0.500	0.500	0.000	0.000	0.000	0.000	0.000	0.000	0.000
2.10	0.00158748	0.000	0.349	0.651	0.000	0.000	0.000	0.000	0.000	0.000	0.000
2.15	0.00166442	0.000	0.251	0.749	0.000	0.000	0.000	0.000	0.000	0.000	0.000
2.20	0.00174178	0.000	0.145	0.854	0.001	0.000	0.000	0.000	0.000	0.000	0.000
2.25	0.00181931	0.000	0.117	0.879	0.004	0.000	0.000	0.000	0.000	0.000	0.000
2.30	0.00189669	0.000	0.060	0.920	0.020	0.000	0.000	0.000	0.000	0.000	0.000
2.35	0.00197363	0.000	0.024	0.925	0.051	0.000	0.000	0.000	0.000	0.000	0.000
2.40	0.00204982	0.000	0.010	0.873	0.117	0.000	0.000	0.000	0.000	0.000	0.000
2.45	0.00212492	0.000	0.005	0.785	0.210	0.000	0.000	0.000	0.000	0.000	0.000
2.50	0.00219862	0.000	0.006	0.657	0.337	0.000	0.000	0.000	0.000	0.000	0.000
2.55	0.00227058	0.000	0.000	0.542	0.458	0.000	0.000	0.000	0.000	0.000	0.000
2.60	0.00234047	0.000	0.000	0.418	0.582	0.000	0.000	0.000	0.000	0.000	0.000
2.65	0.00240795	0.000	0.000	0.256	0.742	0.002	0.000	0.000	0.000	0.000	0.000
2.70	0.00247270	0.000	0.000	0.170	0.826	0.004	0.000	0.000	0.000	0.000	0.000
2.75	0.00253439	0.000	0.000	0.118	0.870	0.012	0.000	0.000	0.000	0.000	0.000
2.80	0.00259273	0.000	0.000	0.054	0.916	0.030	0.000	0.000	0.000	0.000	0.000

Energy (MeV)	GF	L1	L2	L3	L4	L5	L6	L7	L8	L9	L10
2.85	0.00274550	0.000	0.000	0.032	0.896	0.072	0.000	0.000	0.000	0.000	0.000
2.90	0.00283987	0.000	0.000	0.013	0.833	0.154	0.000	0.000	0.000	0.000	0.000
2.95	0.00293047	0.000	0.000	0.005	0.757	0.238	0.000	0.000	0.000	0.000	0.000
3.00	0.00301752	0.000	0.000	0.004	0.677	0.319	0.000	0.000	0.000	0.000	0.000
3.05	0.00310121	0.000	0.000	0.001	0.517	0.481	0.001	0.000	0.000	0.000	0.000
3.10	0.00318173	0.000	0.000	0.001	0.387	0.612	0.000	0.000	0.000	0.000	0.000
3.15	0.00325926	0.000	0.000	0.000	0.257	0.742	0.001	0.000	0.000	0.000	0.000
3.20	0.00333395	0.000	0.000	0.000	0.174	0.822	0.004	0.000	0.000	0.000	0.000
3.25	0.00340595	0.000	0.000	0.000	0.094	0.899	0.007	0.000	0.000	0.000	0.000
3.30	0.00347540	0.000	0.000	0.000	0.073	0.886	0.041	0.000	0.000	0.000	0.000
3.35	0.00354243	0.000	0.000	0.000	0.033	0.898	0.069	0.000	0.000	0.000	0.000
3.40	0.00360716	0.000	0.000	0.000	0.019	0.841	0.140	0.000	0.000	0.000	0.000
3.45	0.00366970	0.000	0.000	0.000	0.011	0.774	0.215	0.000	0.000	0.000	0.000
3.50	0.00373016	0.000	0.000	0.000	0.003	0.662	0.335	0.000	0.000	0.000	0.000
3.55	0.00378863	0.000	0.000	0.000	0.003	0.517	0.480	0.000	0.000	0.000	0.000
3.60	0.00384522	0.000	0.000	0.000	0.000	0.362	0.638	0.000	0.000	0.000	0.000
3.65	0.00390001	0.000	0.000	0.000	0.000	0.265	0.732	0.003	0.000	0.000	0.000
3.70	0.00395307	0.000	0.000	0.000	0.000	0.177	0.816	0.007	0.000	0.000	0.000
3.75	0.00400450	0.000	0.000	0.000	0.000	0.113	0.868	0.019	0.000	0.000	0.000
3.80	0.00405435	0.000	0.000	0.000	0.000	0.054	0.905	0.041	0.000	0.000	0.000
3.85	0.00410271	0.000	0.000	0.000	0.000	0.033	0.874	0.093	0.000	0.000	0.000
3.90	0.00414963	0.000	0.000	0.000	0.000	0.027	0.820	0.153	0.000	0.000	0.000
3.95	0.00419517	0.000	0.000	0.000	0.000	0.006	0.753	0.241	0.000	0.000	0.000
4.00	0.00423940	0.000	0.000	0.000	0.000	0.005	0.631	0.364	0.000	0.000	0.000
4.05	0.00428237	0.000	0.000	0.000	0.000	0.003	0.510	0.487	0.000	0.000	0.000
4.10	0.00432412	0.000	0.000	0.000	0.000	0.001	0.391	0.608	0.000	0.000	0.000
4.15	0.00436472	0.000	0.000	0.000	0.000	0.000	0.265	0.735	0.000	0.000	0.000
4.20	0.00440420	0.000	0.000	0.000	0.000	0.000	0.170	0.830	0.000	0.000	0.000
4.25	0.00444261	0.000	0.000	0.000	0.000	0.000	0.124	0.876	0.000	0.000	0.000
4.30	0.00447999	0.000	0.000	0.000	0.000	0.000	0.049	0.951	0.000	0.000	0.000
4.35	0.00451638	0.000	0.000	0.000	0.000	0.000	0.038	0.962	0.000	0.000	0.000
4.40	0.00455181	0.000	0.000	0.000	0.000	0.000	0.019	0.981	0.000	0.000	0.000
4.45	0.00458634	0.000	0.000	0.000	0.000	0.000	0.011	0.989	0.000	0.000	0.000
4.50	0.00461997	0.000	0.000	0.000	0.000	0.000	0.007	0.993	0.000	0.000	0.000
4.55	0.00465276	0.000	0.000	0.000	0.000	0.000	0.002	0.997	0.001	0.000	0.000
4.60	0.00468474	0.000	0.000	0.000	0.000	0.000	0.000	0.999	0.001	0.000	0.000
4.65	0.00471592	0.000	0.000	0.000	0.000	0.000	0.000	0.997	0.003	0.000	0.000
4.70	0.00474634	0.000	0.000	0.000	0.000	0.000	0.000	0.986	0.014	0.000	0.000
4.75	0.00477602	0.000	0.000	0.000	0.000	0.000	0.000	0.959	0.041	0.000	0.000
4.80	0.00480500	0.000	0.000	0.000	0.000	0.000	0.000	0.933	0.067	0.000	0.000
4.85	0.00483329	0.000	0.000	0.000	0.000	0.000	0.000	0.881	0.119	0.000	0.000
4.90	0.00486092	0.000	0.000	0.000	0.000	0.000	0.000	0.796	0.204	0.000	0.000
4.95	0.00488792	0.000	0.000	0.000	0.000	0.000	0.000	0.698	0.302	0.000	0.000

Energy (MeV)	GF	L1	L2	L3	L4	L5	L6	L7	L8	L9	L10
5.00	0.00491429	0.000	0.000	0.000	0.000	0.000	0.000	0.618	0.382	0.000	0.000
5.05	0.00494006	0.000	0.000	0.000	0.000	0.000	0.000	0.473	0.527	0.000	0.000
5.10	0.00496526	0.000	0.000	0.000	0.000	0.000	0.000	0.389	0.611	0.000	0.000
5.15	0.00498990	0.000	0.000	0.000	0.000	0.000	0.000	0.287	0.713	0.000	0.000
5.20	0.00501400	0.000	0.000	0.000	0.000	0.000	0.000	0.177	0.823	0.000	0.000
5.25	0.00503757	0.000	0.000	0.000	0.000	0.000	0.000	0.141	0.859	0.000	0.000
5.30	0.00506064	0.000	0.000	0.000	0.000	0.000	0.000	0.089	0.911	0.000	0.000
5.35	0.00508321	0.000	0.000	0.000	0.000	0.000	0.000	0.043	0.957	0.000	0.000
5.40	0.00510530	0.000	0.000	0.000	0.000	0.000	0.000	0.032	0.968	0.000	0.000
5.45	0.00512694	0.000	0.000	0.000	0.000	0.000	0.000	0.016	0.984	0.000	0.000
5.50	0.00514812	0.000	0.000	0.000	0.000	0.000	0.000	0.007	0.992	0.001	0.000
5.55	0.00516887	0.000	0.000	0.000	0.000	0.000	0.000	0.002	0.997	0.001	0.000
5.60	0.00518920	0.000	0.000	0.000	0.000	0.000	0.000	0.001	0.991	0.008	0.000
5.65	0.00520911	0.000	0.000	0.000	0.000	0.000	0.000	0.001	0.985	0.014	0.000
5.70	0.00522863	0.000	0.000	0.000	0.000	0.000	0.000	0.002	0.969	0.029	0.000
5.75	0.00524777	0.000	0.000	0.000	0.000	0.000	0.000	0.000	0.945	0.055	0.000
5.80	0.00526652	0.000	0.000	0.000	0.000	0.000	0.000	0.000	0.925	0.075	0.000
5.85	0.00528492	0.000	0.000	0.000	0.000	0.000	0.000	0.000	0.848	0.152	0.000
5.90	0.00530295	0.000	0.000	0.000	0.000	0.000	0.000	0.000	0.800	0.200	0.000
5.95	0.00532065	0.000	0.000	0.000	0.000	0.000	0.000	0.000	0.676	0.324	0.000
6.00	0.00533800	0.000	0.000	0.000	0.000	0.000	0.000	0.000	0.595	0.405	0.000
6.05	0.00535504	0.000	0.000	0.000	0.000	0.000	0.000	0.000	0.489	0.511	0.000
6.10	0.00537175	0.000	0.000	0.000	0.000	0.000	0.000	0.000	0.396	0.604	0.000
6.15	0.00538815	0.000	0.000	0.000	0.000	0.000	0.000	0.000	0.292	0.708	0.000
6.20	0.00540426	0.000	0.000	0.000	0.000	0.000	0.000	0.000	0.209	0.791	0.000
6.25	0.00542007	0.000	0.000	0.000	0.000	0.000	0.000	0.000	0.149	0.851	0.000
6.30	0.00543560	0.000	0.000	0.000	0.000	0.000	0.000	0.000	0.095	0.905	0.000
6.35	0.00545085	0.000	0.000	0.000	0.000	0.000	0.000	0.000	0.066	0.934	0.000
6.40	0.00546583	0.000	0.000	0.000	0.000	0.000	0.000	0.000	0.041	0.959	0.000
6.45	0.00548055	0.000	0.000	0.000	0.000	0.000	0.000	0.000	0.032	0.968	0.000
6.50	0.00549501	0.000	0.000	0.000	0.000	0.000	0.000	0.000	0.009	0.991	0.000
6.55	0.00550921	0.000	0.000	0.000	0.000	0.000	0.000	0.000	0.008	0.992	0.000
6.60	0.00552318	0.000	0.000	0.000	0.000	0.000	0.000	0.000	0.002	0.998	0.000
6.65	0.00553691	0.000	0.000	0.000	0.000	0.000	0.000	0.000	0.001	0.999	0.000
6.70	0.00555040	0.000	0.000	0.000	0.000	0.000	0.000	0.000	0.001	0.999	0.000
6.75	0.00556367	0.000	0.000	0.000	0.000	0.000	0.000	0.000	0.001	0.999	0.000
6.80	0.00557672	0.000	0.000	0.000	0.000	0.000	0.000	0.000	0.000	1.000	0.000
6.85	0.00558965	0.000	0.000	0.000	0.000	0.000	0.000	0.000	0.000	1.000	0.000
6.90	0.00560217	0.000	0.000	0.000	0.000	0.000	0.000	0.000	0.000	1.000	0.000
6.95	0.00561459	0.000	0.000	0.000	0.000	0.000	0.000	0.000	0.000	1.000	0.000
7.00	0.00562680	0.000	0.000	0.000	0.000	0.000	0.000	0.000	0.000	1.000	0.000
7.05	0.00563882	0.000	0.000	0.000	0.000	0.000	0.000	0.000	0.000	1.000	0.000
7.10	0.00565065	0.000	0.000	0.000	0.000	0.000	0.000	0.000	0.000	1.000	0.000

Energy (MeV)	GF	L1	L2	L3	L4	L5	L6	L7	L8	L9	L10
7.15	0.00566229	0.000	0.000	0.000	0.000	0.000	0.000	0.000	0.000	1.000	0.000
7.20	0.00567375	0.000	0.000	0.000	0.000	0.000	0.000	0.000	0.000	1.000	0.000
7.25	0.00568503	0.000	0.000	0.000	0.000	0.000	0.000	0.000	0.000	1.000	0.000
7.30	0.00569613	0.000	0.000	0.000	0.000	0.000	0.000	0.000	0.000	1.000	0.000
7.35	0.00570707	0.000	0.000	0.000	0.000	0.000	0.000	0.000	0.000	0.999	0.001
7.40	0.00571783	0.000	0.000	0.000	0.000	0.000	0.000	0.000	0.000	1.000	0.000
7.45	0.00572844	0.000	0.000	0.000	0.000	0.000	0.000	0.000	0.000	0.999	0.001
7.50	0.00573888	0.000	0.000	0.000	0.000	0.000	0.000	0.000	0.000	0.997	0.003
7.55	0.00574917	0.000	0.000	0.000	0.000	0.000	0.000	0.000	0.000	0.994	0.006
7.60	0.00575930	0.000	0.000	0.000	0.000	0.000	0.000	0.000	0.000	0.993	0.007
7.65	0.00576929	0.000	0.000	0.000	0.000	0.000	0.000	0.000	0.000	0.979	0.021
7.70	0.00577913	0.000	0.000	0.000	0.000	0.000	0.000	0.000	0.000	0.950	0.050
7.75	0.00578882	0.000	0.000	0.000	0.000	0.000	0.000	0.000	0.000	0.944	0.056
7.80	0.00579838	0.000	0.000	0.000	0.000	0.000	0.000	0.000	0.000	0.875	0.125
7.85	0.00580780	0.000	0.000	0.000	0.000	0.000	0.000	0.000	0.000	0.834	0.166
7.90	0.00581708	0.000	0.000	0.000	0.000	0.000	0.000	0.000	0.000	0.788	0.212
7.95	0.00582623	0.000	0.000	0.000	0.000	0.000	0.000	0.000	0.000	0.692	0.308
8.00	0.00583526	0.000	0.000	0.000	0.000	0.000	0.000	0.000	0.000	0.644	0.356
8.05	0.00584415	0.000	0.000	0.000	0.000	0.000	0.000	0.000	0.000	0.543	0.457
8.10	0.00585293	0.000	0.000	0.000	0.000	0.000	0.000	0.000	0.000	0.465	0.535
8.15	0.00586158	0.000	0.000	0.000	0.000	0.000	0.000	0.000	0.000	0.315	0.685
8.20	0.00587011	0.000	0.000	0.000	0.000	0.000	0.000	0.000	0.000	0.275	0.725
8.25	0.00587853	0.000	0.000	0.000	0.000	0.000	0.000	0.000	0.000	0.197	0.803
8.30	0.00588683	0.000	0.000	0.000	0.000	0.000	0.000	0.000	0.000	0.169	0.831
8.35	0.00589502	0.000	0.000	0.000	0.000	0.000	0.000	0.000	0.000	0.114	0.886
8.40	0.00590310	0.000	0.000	0.000	0.000	0.000	0.000	0.000	0.000	0.075	0.925
8.45	0.00591107	0.000	0.000	0.000	0.000	0.000	0.000	0.000	0.000	0.051	0.949
8.50	0.00591894	0.000	0.000	0.000	0.000	0.000	0.000	0.000	0.000	0.029	0.971
8.55	0.00592670	0.000	0.000	0.000	0.000	0.000	0.000	0.000	0.000	0.014	0.986
8.60	0.00593436	0.000	0.000	0.000	0.000	0.000	0.000	0.000	0.000	0.015	0.985
8.65	0.00594193	0.000	0.000	0.000	0.000	0.000	0.000	0.000	0.000	0.004	0.996
8.70	0.00594939	0.000	0.000	0.000	0.000	0.000	0.000	0.000	0.000	0.000	1.000
8.75	0.00595676	0.000	0.000	0.000	0.000	0.000	0.000	0.000	0.000	0.000	1.000
8.80	0.00596403	0.000	0.000	0.000	0.000	0.000	0.000	0.000	0.000	0.000	1.000
8.85	0.00597122	0.000	0.000	0.000	0.000	0.000	0.000	0.000	0.000	0.000	1.000
8.90	0.00597831	0.000	0.000	0.000	0.000	0.000	0.000	0.000	0.000	0.001	0.999
8.95	0.00598531	0.000	0.000	0.000	0.000	0.000	0.000	0.000	0.000	0.000	1.000
9.00	0.00599222	0.000	0.000	0.000	0.000	0.000	0.000	0.000	0.000	0.000	1.000
9.05	0.00599905	0.000	0.000	0.000	0.000	0.000	0.000	0.000	0.000	0.000	1.000
9.10	0.00600580	0.000	0.000	0.000	0.000	0.000	0.000	0.000	0.000	0.000	1.000
9.15	0.00601246	0.000	0.000	0.000	0.000	0.000	0.000	0.000	0.000	0.000	1.000
9.20	0.00601904	0.000	0.000	0.000	0.000	0.000	0.000	0.000	0.000	0.000	1.000
9.25	0.00602554	0.000	0.000	0.000	0.000	0.000	0.000	0.000	0.000	0.000	1.000

Energy (MeV)	GF	L1	L2	L3	L4	L5	L6	L7	L8	L9	L10
9.30	0.00603196	0.000	0.000	0.000	0.000	0.000	0.000	0.000	0.000	0.000	0.999
9.35	0.00603830	0.000	0.000	0.000	0.000	0.000	0.000	0.000	0.000	0.000	0.999
9.40	0.00604457	0.000	0.000	0.000	0.000	0.000	0.000	0.000	0.000	0.000	1.000
9.45	0.00605077	0.000	0.000	0.000	0.000	0.000	0.000	0.000	0.000	0.000	0.997
9.50	0.00605689	0.000	0.000	0.000	0.000	0.000	0.000	0.000	0.000	0.000	0.992
9.55	0.00606293	0.000	0.000	0.000	0.000	0.000	0.000	0.000	0.000	0.000	0.994
9.60	0.00606891	0.000	0.000	0.000	0.000	0.000	0.000	0.000	0.000	0.000	0.978
9.65	0.00607482	0.000	0.000	0.000	0.000	0.000	0.000	0.000	0.000	0.000	0.964
9.70	0.00608066	0.000	0.000	0.000	0.000	0.000	0.000	0.000	0.000	0.000	0.946
9.75	0.00608643	0.000	0.000	0.000	0.000	0.000	0.000	0.000	0.000	0.000	0.928
9.80	0.00609214	0.000	0.000	0.000	0.000	0.000	0.000	0.000	0.000	0.000	0.891
9.85	0.00609778	0.000	0.000	0.000	0.000	0.000	0.000	0.000	0.000	0.000	0.833
9.90	0.00610336	0.000	0.000	0.000	0.000	0.000	0.000	0.000	0.000	0.000	0.806
9.95	0.00610888	0.000	0.000	0.000	0.000	0.000	0.000	0.000	0.000	0.000	0.740
10.00	0.00611433	0.000	0.000	0.000	0.000	0.000	0.000	0.000	0.000	0.000	0.659
10.05	0.00611972	0.000	0.000	0.000	0.000	0.000	0.000	0.000	0.000	0.000	0.544
10.10	0.00612505	0.000	0.000	0.000	0.000	0.000	0.000	0.000	0.000	0.000	0.510
10.15	0.00613033	0.000	0.000	0.000	0.000	0.000	0.000	0.000	0.000	0.000	0.424
10.20	0.00613554	0.000	0.000	0.000	0.000	0.000	0.000	0.000	0.000	0.000	0.348
10.25	0.00614070	0.000	0.000	0.000	0.000	0.000	0.000	0.000	0.000	0.000	0.262
10.30	0.00614580	0.000	0.000	0.000	0.000	0.000	0.000	0.000	0.000	0.000	0.218
10.35	0.00615085	0.000	0.000	0.000	0.000	0.000	0.000	0.000	0.000	0.000	0.147
10.40	0.00615584	0.000	0.000	0.000	0.000	0.000	0.000	0.000	0.000	0.000	0.106
10.45	0.00616078	0.000	0.000	0.000	0.000	0.000	0.000	0.000	0.000	0.000	0.079
10.50	0.00616567	0.000	0.000	0.000	0.000	0.000	0.000	0.000	0.000	0.000	0.051